Applied Energy 340 (2023) 120957

Contents lists available at ScienceDirect

Applied Energy

journal homepage: www.elsevier.com/locate/apenergy

Enhancing flexibility for climate change using seasonal energy storage (aquifer thermal energy storage) in distributed energy systems

A.T.D. Perera [a,b,*], Kenichi Soga [c], Yujie Xu [b], Peter S. Nico [d], Tianzhen Hong [b]

[a] *Andlinger Center For Energy And Environment, Princeton University, NJ 08540, United States*
[b] *Building Technology and Urban Systems Division, Lawrence Berkeley National Laboratory, 1, Cyclotron Road, Berkeley, CA, 94720, United States*
[c] *Department of Civil and Environmental Engineering, University of California Berkeley, Berkeley, CA, United States*
[d] *Earth and Environmental Sciences Area, Lawrence Berkeley National Laboratory, Berkeley, CA 94720, United States*

HIGHLIGHTS

- A novel computational model to distributed energy hubs with ATES.
- Stochastic optimization of energy hubs with long term thermal storage.
- Assess the technoeconomic feasibility of ATES.
- Assess the role of ATES to enhance flexibility for future climate variations.

ARTICLE INFO

Keywords:
Long-term/seasonal storage
Distributed multi-energy systems
Stochastic optimization
Geothermal energy
Aquifer thermal energy storage
ATES
Climate change

ABSTRACT

Long-term energy storage is expected to play a vital role in the deep decarbonization of building energy sectors, while enhancing the flexibility of buildings to withstand future climate variations. However, it is challenging to design distributed multi-energy systems (DMES) while taking into account the uncertainties introduced by climate change, since stochastic optimization of such systems is difficult. The present study introduces a stochastic optimization model to address this bottleneck, taking into account DMES including aquifer thermal energy storage (ATES) as the long-term thermal storage. For the first time, a novel optimization algorithm links ATES with the DMES optimization model with the support of a simplified geotechnical model. Subsequently, a case study was conducted, focusing on a residential district in Chicago where the impact of future climate condition, energy demand, and solar and wind energy potentials were evaluated using Weather Research and Forecasting (WRF) data (up to 2080) and the EnergyPlus model. The study revealed that ATES is an attractive way to improve the renewable energy penetration level and minimize the dependence on fossil fuels with reasonable support from the grid to assist the fluctuations in both demand and generation. Furthermore, ATES notably reduces fuel consumption and dependence while greatly enhancing the flexibility of the energy system to withstand fluctuations in demand and renewable energy generation brought by future climate variations. These qualities will make ATES an important part of distributed energy systems, even though it is not currently the lowest cost alternative due to lack of technology maturity. The design platform introduced in the present study can be used to design DMES enhancing flexibility to accommodate future climate variations.

1. Introduction

Decarbonizing the energy sector is a main challenge to be faced during climate change mitigation [1]. Integration of renewable energy technologies to replace carbon intensive means of power generation based of fossil fuel resources is essential. At the same time, market uncertainties of fossil fuels due to geopolitical activities encourage a move to renewable energy technologies such as solar and wind. Therefore, a significant increase in the penetration levels of solar photovoltaic (PV) and wind technologies is observed throughout the world. For example, China alone has installed 53 GW (GW) of solar PV during 2021 [2]. However, when compared to the national level targets required for 1.5 °C scenarios, the trends for both solar PV and wind integration

---

* Corresponding author.
E-mail address: ap0472@princeton.edu (A.T.D. Perera).

https://doi.org/10.1016/j.apenergy.2023.120957
Received 19 October 2022; Received in revised form 6 February 2023; Accepted 5 March 2023

Nomenclature

Abbreviations

ATES	aquifer thermal energy storage
CHP	combined heat and power
DMES	distributed multi-energy systems
H2	Hydrogen
ICG	internal combustion generator
MILP	mixed integer linear programming
SPV/PV	solar photovoltaic
WRF	Weather Research and Forecasting

Sets

T	set of time steps
Ω	set of scenarios

Parameters of the energy model

$AC_{t,s}$	electricity load for the air-conditioning
$A_{overlap}$	overlap area of ATES
A_{SPV}	area of a single SPV panel
c_{aq}	heat capacity of the aquifer
$\mathrm{C_{bat}}$	capacity of battery bank
$COP_{t,s}^{HP,H}$	coefficient of performance-heat pump
$COP_{t,s}^{Ref,C}$	coefficient of performance - cooling cycle
c_w	volumetric heat capacity of water
c_s	volumetric heat capacity of solids
$\mathrm{ELT_{t,s}}$	electricity load demand
$\mathrm{G_{t,s}^{\beta}}$	global solar radiation on a tilted plane
$HP_{t,s}^{ATES,H}$	electricity consumption ATES heat pump
$I_{t,s}^{Bat,\max}$	maximum current from battery bank
L	thickness of the aquifer
LPS^H	loss of heating demand
$\mathrm{LPS^E}$	loss of electricity demand
LPS^C	loss of cooling demand
n	porosity of the aquifer
N_{SPV}	number of SPV panels
$P_{t,s}^{Bat-Max}$	maximum power flow from the battery
$P_{t,s}^{FG-Max}$	maximum power that can be taken from the grid
$P_{\max}^{ICC}$	maximum ICG's power output
$P_{\min}^{IGG}$	minimum ICG's power output
P_R	rated power of the wind turbine
$P_{t,s}^{RE}$	renewable power generation
$P_{t,s}^{SPV}$	solar power generation
$P_{t,s}^{W}$	wind turbine power generation
N_w	number of wind turbines
$Q_{t,s}^{C,B}$	cooling demand of the building cluster
$Q_{t,s}^{H.B}$	heating demand of the building cluster
$\mathrm{R_h}$	radius of the hydraulic front
$\mathrm{R_{th}}$	radius of the heat front
$Ref_{t,\,s}^{ATES,C}$	electricity consumption used to cool the ATES
$s\ (\forall s \in \Omega)$	scenario
SOC	state of charge
$SOC_{t+1,\,s}^{ATES,C}$	state of charge of the cold well
$SOC_{t+1,\,s}^{ATES,H}$	state of charge of the hot well
$t\ (\forall t \in T)$	time step
Δt	time step for charge/discharge
$\Delta t_{Seasonal}^{ATES}$	number of hourly time steps for the discharge season
tsp	storage period
u^*	groundwater flow rate
V^{Bat}	voltage across the battery bank
v_{CI}	cut-in wind speed of the wind turbine
v_{CO}	cut-off wind speed of the wind turbine
$\mathrm{V_{in}}$	fluid of volume injected into the aquifer
v_R	rated wind speed of the wind turbine
α^c	fraction of the cooling demand supplied by the ATES
α^H	fraction of thermal energy provided by ATES
$\eta^{ATES,rec}$	recovery efficiency of ATES
$\eta_{t,s}^{Bat,ts}$	round-cycle efficiency of battery bank
$\eta_{t,s}^{SPV}$	energy efficiency of the SPV panels
$\eta_{\mathrm{wind\text{-}losses}}$	other wind turbine losses
$\mathrm{K}_{t,s}$	electricity consumption of the auxiliary devices
$\alpha_{t,s}^{bat}$	self-discharge coefficient of battery bank
$\sigma_{t,s}^{ATES,H}$	self-discharge of the hot well
$\sigma_{t,s}^{ATES,C}$	self-discharge of cold well
ψ_s	probability of scenario s

Parameters of the cost model

$\mathrm{CRF_c}$	capital recovery factor
ICC	initial capital cost
LEC	levelized energy cost
PRI	real interest rate
$\mathrm{OM^{fixed}}$	fixed operation and maintenance cost
$\mathrm{OM^{variable}}$	variable operation and maintenance cost

become challenging [3]. The countries that have already reached higher penetration levels of wind and solar PV are gradually slowing the integration process, following an S curve [4]. Therefore, facilitating solar PV and wind integration is essential to reach 1.5 °C climate targets.

The intermittent nature of solar and wind energy is the main hurdle that must be addressed during the integration of these technologies. Both solar irradiation and wind speed are governed by weather conditions. The potential of solar and wind energy does not follow a pattern that enables them to meet continual energy demand, so they require additional support to store energy. Therefore, energy storage has become essential to support the integration of renewable energy technologies. Energy storage has been widely discussed in relation to transportation, industry, and the building sector [5]. Already the transportation sector is going through a revolution to replace inefficient and environmentally expensive internal combustion engines with vehicles supported by battery and hydrogen storage [6]. Similarly, grid storage and domestic electricity storage have been widely discussed, especially with the introduction of new tariff systems [7]. The significant cost reductions during recent years have made battery storage more popular in many sectors [8]. However, these developments must move beyond the electricity sector and enable energy storage technologies to facilitate decarbonization of the building sector, which constitutes up to 40% of energy demand [9]. Thermal energy storage can address needs such as the higher energy demand for heating during the winter to hot water demand from solar heaters during the night [9]. Therefore, short-term (daily) as well as long-term (seasonal) energy storage considerations play a vital role in the energy transition.

Long-term storage plays a key role in enhancing renewable energy penetration levels, especially when reaching ambitious renewable energy targets [10]. Most of the recent studies in this area focus on long-term storage technologies such as pumped hydropower, power to hydrogen, and compressed air [11]. However, there are limitations in solely limiting the scope of these technologies to the electricity sector. For example, pumped hydro storage is highly sensitive to climate change

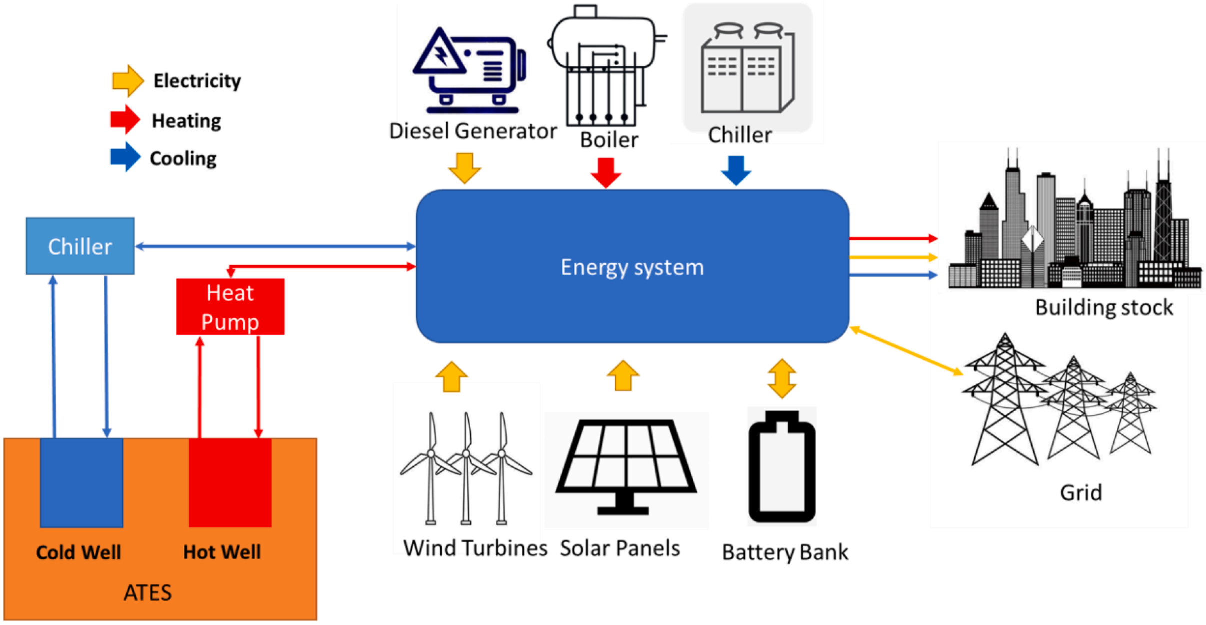

Fig. 1. Outliner of the energy system.

[12], and the storage capacity is limited when considering global requirements. On the other hand, heating demand does not align with the availability to solar energy potential. Therefore, thermal energy storage is vital to enhance the solar energy integration levels. Therefore, it is important to move into multi-storage solutions that cover both electricity and heating sectors, especially in deep decarbonization scenarios [10,13]. Guo et al. [14] showed the renewable energy penetration level could be improved up to 69% by using such multi-energy systems. More important, a significant portion of the thermal energy demand can be generated within the site of the distributed energy systems with the support of long-term storage. [15]. Further, Zeyen et al. [16] showed that long-term storage, along with building renovation and heat pumps, can reduce the total cost of the energy system up to 17%. However, incorporating consideration of long-term storage within a multi-energy system domain makes it quite challenging to perform optimization.

Several studies have focused on the optimal sizing of multi-energy systems, including long-term storage. For example Heijde et al. optimized a solar energy district with long-term thermal energy storage [17]. They used a bi-level optimization algorithm where the primary level, with mixed integer linear programming (MILP), was used for dispatch strategy, and the secondary level, with a genetic algorithm, was used for design optimization. Gabrielli optimized a multi-energy system with seasonal hydrogen storage using MILP [18]. Murrey et al. assessed the impact of both short- and long-term energy storage (specifically focusing at power to Hydrogen (H2) and showed that long-term storage has the potential to shift renewable surpluses in the summer towards demand later in the year. According to Petkov et al. [19], uncertainty plays a vital role when designing distributed energy systems with long-term energy storage. Li [20] et al. performed stochastic optimization of a heterogeneous energy storage system operation. Optimizing energy systems with long-term storage while taking into account the uncertainties is a challenging task. Quiroz and Strunz [21] introduced a distributed algorithm based on Dantzig-Wolfe decomposition [22] to optimize a distributed energy system with renewable energy technologies. According to Quiroz and Strunz [21], the optimization process took eight days, even after limiting the dispatch strategy to be four representative weeks of the year. Limiting the represented period to under a year makes it challenging to assess the impact of climate change where simulation-based formulations of objective functions need to be formulated to consider an entire year [23,24]. Furthermore, thermal storage is not considered in the system design, which again plays a major role when considering the impact of climate change. Therefore, it is important to develop computational methods to perform design optimization of distributed energy systems that take into account sectors such as heating and cooling along with the electricity while addressing the bottlenecks in the present state of the art (one objective of this study).

To help develop distributed multi-energy systems that can withstand the fluctuations introduced by future climate variations and enhance renewable energy penetration, the present study focused on a distributed energy system configuration that includes long-term thermal energy storage. Borehole and aquifer thermal energy storage (ATES) have been well known subsurface technologies that can operate as seasonal storage technologies [9]. Although both of these technologies have shown economic viability, less attention has been given to ATES historically [9]. However, more recently, much attention has been given to ATES by both the geothermal and energy storage communities, since it has shown the potential to be an economically competitive long-term energy storage technique [25]. A number of aspects related to ATES have been investigated in the present state of the art. Numerical models have been developed to assess the thermal performances of ATES. These models have focused on assessing the energy recovery efficiency and thermal performance of ATES under different ground conditions [26]. Subsurface thermo-hydro models are often coupled with thermal system models in order to achieve this task. Techno-economic assessments have been performed to assess the viability of ATES under different conditions. These studies have reflected the economic potential of ATES up to a certain level [27,28].

Integration of ATES into distributed energy systems such as energy hubs has been discussed recently [29–31]. Rostampour and Tamas [29] and Rostampor et al. [29] have discussed the optimal operation of ATES in distributed energy systems, which clearly demonstrate the potential of ATES to be integrated into distributed energy systems. The optimal operation of a distributed energy system highly depends on the system's configuration, including its capacity for PV panels, wind turbines, a combined heat and power (CHP) system, and other storage techniques, such as battery banks [32]. More important, renewable energy integration could help to withstand certain operational costs of ATES, which can help to increase their market penetration. However, optimal design of distributed energy systems with ATES is a challenging task. The

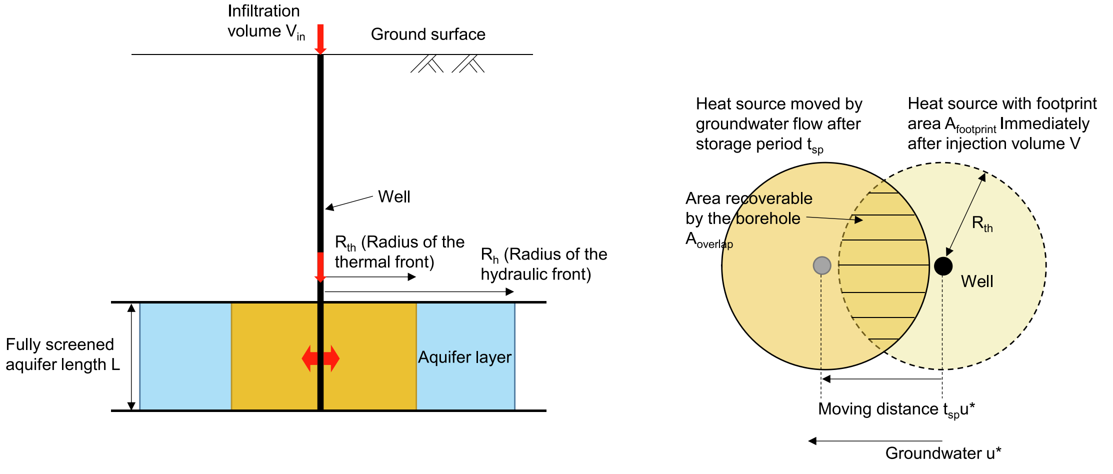

(a) Side view (without ground water flow) (b) Plan view (with ground water flow)

Fig. 2. (a) and (b), respectively, present a side view and a plan view of the aquifer thermal energy storage.

complex coupling between subsurface thermo-hydro behaviour and ATES operation makes it quite challenging to integrate ATES into a distributed energy system. The subsurface characteristics that influence the thermal performance of ATES are often obtained from numerical models that are not compatible with energy system optimization models. To the best of the authors' knowledge, design optimization (system sizing) of distributed energy systems with ATES has not been performed before. The optimization problem becomes more challenging when considering the future climate variations due to climate change, which will favour the integration of ATES. Therefore, a reasonable research gap must be addressed to facilitate ATES integration into distributed energy systems.

To address these bottlenecks in the present state of the art, this study focused on addressing the following objectives:

- Develop a computational model integrating ATES into the distributed energy system that can facilitate energy system optimization.
- Extend the computation model to perform stochastic optimization considering the uncertainties brought by future climate variations and building operation.
- Perform multi-objective optimization, considering aspects such as cost, grid integration level, and fuel consumption.
- Assess the impact of ATES on renewable energy integration and battery storage sizing.
- Assess the impact of ATES on the performance indicators such as cost, grid integration level, and flexibility.

The manuscript is organized as follows: Section 2 presents the computational model developed in the study. Section 3 presents the case study, including the derivation of demand profiles. Section 4 presents the results of the Pareto optimization, followed by a comprehensive assessment.

2. Techno-economic model for the distributed energy system

The techno-economic model presents a brief overview of the energy system model used in the present study. A stochastic model was used to account for uncertainties brought by the changes in energy demand and renewable energy generation.

2.1. Outline of the distributed energy system

The distributed energy system that can cater the multi energy services such as electricity, heating and cooling with the support of the renewable energy technologies generated locally is considered in this study (Fig. 1). The energy hub concept has been widely used to consider such distributed energy systems catering multi energy services. The present study uses the same concept and an extension to the energy hub models developed previously. The energy hub consists of renewable energy technologies such as solar PV and wind turbines. Both electrical and thermal energy storage technologies were considered. The battery bank operated as the electricity storage while the ATES operated as the thermal storage. The boiler and chiller were used as alternative heating and cooling options. In addition, a chiller and heat pump were connected with the ATES to match the temperatures between the well and the building energy system. The internal combustion generator (ICG) operated as the dispatchable energy source. Both the boiler and the ICG were using fossil fuel provided externally. The system was operating in grid integrated mode and included a time-of-use tariff system. Grid curtailments were considered for both injection and purchase of electricity to and from the grid. A limit is set for maximum power that could be injected or purchased from the grid.

2.2. Energy system model

2.2.1. Solar PV generation

Solar PV and wind energy technologies were considered as non-dispatchable renewable energy technologies. The hourly potential for both these technologies were extracted from a climate model. A comprehensive explanation about the method used to extract the climate data is presented in Section 3. Hourly global horizontal irradiation data are extracted from the climate data set, which is used to calculate the global solar radiation on a tilted plane that comprises the solar PV (SPV) panels (i.e., $G^{\beta}_{t,s}$) using an anisotropic diffuse solar radiation model. A comprehensive explanation about the models used to compute the global solar radiation on a tilted plane is presented in Ref. [33]. Finally, hourly solar energy generation ($P^{SPV}_{t,s}$) for time step t ($\forall t \in T$) in scenario s ($\forall s \in \Omega$) (denotes the scenario considered for stochastic optimization) is computed using Eq. (1).

$$P^{SPV}_{t,s} = G^{\beta}_{t,s}\,\eta^{SPV}_{t,s}\,A^{SPV}N^{SPV}, \quad \forall t \in T, \forall s \in \Omega \tag{1}$$

In Eq. (1), A_{SPV} and N_{SPV} represent the area of a single SPV panel, as well as the number of SPV panels. A semi empirical formula proposed by Durisch et al. [34] is used to determine the energy efficiency of the SPV panels ($\eta^{SPV}_{t,s}$). A time series of 8,760 timesteps was considered for the simulation.

2.2.2. *Wind power generation*

A similar approach was used to formulate the power generation from wind turbines ($P^{W}_{t,s}$) according to Eq. (2).

$$P^{W}_{t,s} = \widetilde{P^{W}_{t,s}}(\mathrm{v}_{t,s})\ \mathrm{N}^{\mathrm{w}}\ \eta^{\mathrm{W\,-\,losses}}, \forall t \in T,\ \forall s \in \Omega \tag{2}$$

In Eq. (2), N_w denotes the number of wind turbines that is optimized using the optimization algorithm, $\widetilde{P^{W}_{t,s}}(\mathrm{v}_{t,s})$ denotes power generated by one wind turbine based on the wind speed v, calculated using the power curve, and $\eta_{\text{wind-losses}}$ accounts for other losses that take place in energy conversion.

The power generation from a single wind turbine is computed by using the cubic spline interpolation function with the support of a power curve of the wind turbine given by the manufacturer. Eq. (3) presents the cubic spline interpolation function.

$$\widetilde{P}^{w}_{t,s} = \begin{cases} \widetilde{P}^{w}_{t,s} = 0, & v_{CI} > v_{t,s} \\ \widetilde{P}^{w}_{t,s} = a^{w}_{1} v^{3}_{t,s} + b^{w}_{1} v^{2}_{t,s} + c^{w}_{1} v_{t,s} + d^{w}_{1}, & v_{CI} < v_{t,s} < v_{1} \\ \widetilde{P}^{w}_{t,s} = a^{w}_{2} v^{3}_{t,s} + b^{w}_{2} v^{2}_{t,s} + c^{w}_{2} v_{t,s} + d^{w}_{2}, & v_{1} < v_{t,s} < v_{2} \\ \cdots\cdots\cdots & \\ \cdots\cdots\cdots & \\ \widetilde{P}^{w}_{t,s} = a^{w}_{n} v^{3}_{t,s} + b^{w}_{n} v^{2}_{t,s} + c^{w}_{n} v_{t,s} + d^{w}_{n}, & v_{n-1} < v_{t,s} < v_{n} \\ \widetilde{P}^{w}_{t,s} = P_{R}, & v_{n_s} < v_{t} < v_{CO} \\ \widetilde{P}^{w}_{t,s} = 0, & v_{t,s} > v_{CO} \end{cases} , \forall t \in T,\ \forall s \in \Omega \tag{3}$$

In Eq. (3), respectivelya^{w}_{n},b^{w}_{n},c^{w}_{n}, and d^{w}_{n} denote coefficients of the polynomial function, which vary depending on the "power curve" of the wind turbine. Rated wind speed, cut-in wind speed, cut-off wind speed, and rated power of the wind turbine are respectively presented by v_R, v_{CI}, v_{CO}, and P_R.

2.2.3. *Computational model for the internal combustion generator and boiler*

Two dispatchable energy technologies—an internal combustion generator (ICG) and a boiler were considered in this study. The ICG was used to provide the electricity demand, depending on the dispatch strategy. The fuel consumption of the ICG was formulated based on its operating load.

($P^{ICG}_{t,s}$) according to Eq. (4), taking into account the valve point effect (usually not considered in simple polynomial equations).

$$FC^{ICG}_{t,s} = a^{ICG}_{0} + a^{ICG}_{1} P^{ICG}_{t,s} + a^{ICG}_{2} P^{ICG}_{t,s} + a^{ICG}_{3} \left| \sin\left(a^{ICG}_{4} \left(P^{ICG}_{t,s} - P^{ICG}_{\min} \right) \right) \right|, \forall t \in T,\ \forall s \in \Omega,\ P^{ICG}_{\min} < P^{ICG}_{t,s} < P^{ICG}_{\max} \tag{4}$$

In Eq. (4), $P^{ICG}_{\max}$ and $P^{ICG}_{\min}$ denote the ICG's maximum and minimum power output, respectively. The constants a^{ICG}_{0} to a^{ICG}_{4} are constants that vary depending upon the type of ICG. A similar approach is used to compute the fuel consumption of the boilers.

2.2.4. *Model for the battery bank*

A battery bank and ATES are used for the system's energy storage. The battery bank acts as short-term electricity storage, while the ATES operates as seasonal thermal storage. Both the ATES and the battery bank are modeled using the State of Charge (SOC) model, which helps to determine the charge level available in the energy storage. The SOC of the battery bank is determined using Eq. (5).

$$SOC^{Bat}_{t+1,s} = SOC^{Bat}_{t,s}\left(1 - \sigma^{Bat}_{t,s}\right) + V^{Bat} I^{\,Bat,\max}_{t,s} \Delta t\, \eta^{Bat,ch}_{t,s} \Big/ c^{Bat}, \forall t \in T,\ \forall s \in \Omega,\ SOC^{Bat}_{\min} < SOC^{Bat}_{t+1,\,s} < SOC^{Bat}_{\max} \tag{5}$$

In Eq. (5), $\sigma^{Bat}_{t,s}$ denotes the self-discharge coefficient of the battery bank, which was taken as 0.02% (per hour). C_{bat} and$\eta^{Bat,ch}_{t,s}$, respectively, present the capacity of the battery bank and its round-cycle efficiency.$I^{\,Bat,\max}_{t,s}$,V^{Bat}, and Δt present the maximum current that can be taken, voltage across the battery bank, and time step (taken as one hour), respectively. Based on the number of charge–discharge cycles, the Rain-Flow Algorithm [35] is used to compute the replace time for the battery bank. Finally, replacement time is used to compute the variable maintenance cost of the battery bank.

2.2.5. *Energy flow model for the ATES*

- **Model for the energy storage**

A similar approach based on the State of Charge (SOC) model was used for the ATES. The ATES consists of a hot well and a cool well. The state of charge of the hot well ($SOC^{ATES,H}_{t+1,\,s}$) is determined based on charging from the cooling cycle, self-discharge ($\sigma^{ATES,H}_{t,s}$), and discharge from the heating cycle according to Eq. 6 A. The hot well is charged whenever cooling is performed, where water flow takes place from the cold well to the hot well. Eq. 6 A is formulated when the complete cooling cycle could be achieved without the support of air-conditioning (other operating states are described in the dispatch). $Q^{H,B}_{t,s}$ denotes the heating demand of the building cluster. The ATES can provide only a fraction of the thermal potential required for heating the building cluster. A heat pump is used to provide the rest of the thermal potential (to increase the temperature). The fraction of the thermal energy provided by the ATES is presented byα^{H}, while the fraction of thermal energy provided by the heat pump is 1-α^{H}. α^{H} depends on the temperature of the hot well, the heat pump's operating characteristics, and the building energy system. Similarly, $Q^{C,B}_{t,s}$ andα^{C}, respectively, denote the cooling demand and the fraction of the cooling demand supplied by the ATES ((1-α^{C}) presents the fraction of cooling demand supplied by the refrigeration cycle). The self-discharge ($\sigma^{ATES,H}_{t,s}$) presents the thermal losses that take place from the hot well. Ideally, $\sigma^{ATES,H}_{t,s}$ depends on the state of charge of the hot well. However, numerical models that are used to compute $\sigma^{ATES,H}_{t,s}$ may significantly increase the computational time, which makes it difficult to be used with the optimization algorithms. Therefore, an analytical approach was used in the present study to compute $\sigma^{ATES,H}_{t,s}$ as presented in Eq. 6 B. Recovery efficiency is computed ($\eta^{ATES,Rec}$)in a seasonal manner considering the operation of the ATES. Considering th climate of Chicago a heating season of (tsp) 92 days are considered. Out of the energy stored in the cold well during this period, $\eta^{ATES,Rec}$ can be ustilized during the summer due to the losses take place (the rest is lost due to thermal and flow losses). In this study, we assumed that the thermal losses take place uniformely throughout the year. Therefore, the self-discharge can be $\sigma^{ATES,H}_{t,s}$ (per hour) formulated according to Eq. 6 B, where we assume that the thermal losses take place

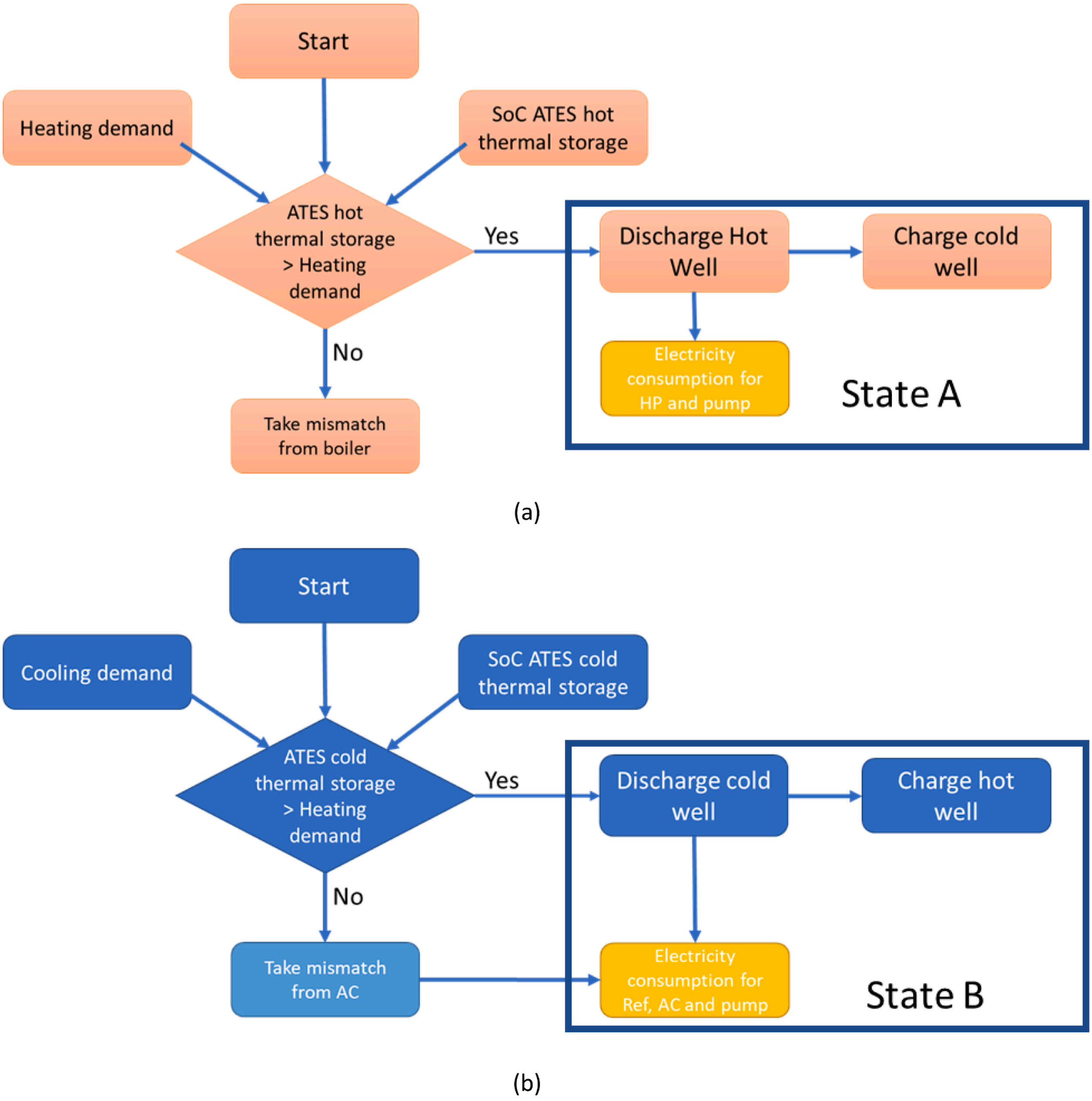

Fig. 3. Primary stage of dispatch strategy providing (a) heating and (b) cooling energy demands.

uniformly throughout the discharge season. In Eq. 6 B, $\Delta t^{ATES}_{Seasonal}$ denotes the hourly time steps for the discharge season (2208 time steps (92x24)). Finally, electricity consumption for the heat pump of the ATES ($HP^{ATES,H}_{t,s}$) is computed using Eq. 6 C. In Eq. 6 C, $COP^{HP,H}_{t,s}$ presents the coefficient of performance of the heat pump, which is taken as a function of temperature as shown in Eq. (6D) where $T_{cond,\ out}$ and $T_{evap,\ in}$ presents the temperatures at the condenser outlet and evaporator inlets. The state of the charge of ATES depends on the operating state of the dispatch strategy. Considering State A marked in Fig. 3 (a) the state of the charge of hotwell can be formulated as Eq. (6A).

$$SOC^{ATES,H}_{t+1,\ s} = SOC^{ATES,H}_{t,\ s}\left(1-\sigma^{ATES,H}_{t,s}\right) - \left(Q^{H,B}_{t,s}\alpha^{H} - Q^{C,B}_{t,s}\alpha^{C}\right)\Big/c^{ATES,H},\ \forall t \in T,\ \forall s \in \Omega,\ SOC^{ATES,H}_{\min} < SOC^{ATES,H}_{t+1,\ s} < c^{ATES,H} \tag{6A}$$

$$\sigma^{ATES,H}_{t,s} = \left(1-\eta^{ATES,Rec}\right)\Big/\Delta t^{ATES}_{Seasonal} \tag{6B}$$

$$HP^{ATES,H}_{t,\ s} = Q^{H,B}_{t,s}\left(1-\alpha^{H}\right)\Big/COP^{HP,H}_{t,s}\ \forall t \in T,\ \forall s \in \Omega,\ 0 < \alpha^{H} < 1 \tag{6C}$$

$$COP^{HP,H}_{t,s} = 7.5 - 0.07\left(T_{cond,out} - T_{evap,in}\right) \tag{6D}$$

A similar approach is taken for the cold well, as presented in Eq. 7 A-C. The state of charge of the cold well ($SOC^{ATES,C}_{t+1,\ s}$) is presented according to Eq. 7 A. Similar to the hot well, the state of charge is determined based on charging from the hot cycle, self-discharge ($\sigma^{ATES,C}_{t,s}$), and discharge from the cool cycle. Eq. 7 A is formulated when the complete hot cycle could be achieved without the support of the boiler (other operating states are described in the dispatch). The ATES can provide only a fraction of the thermal potential required for cooling the building cluster. A cooling cycle is used to provide the rest of the thermal potential (reduce the temperature). The fraction of the thermal energy removed by the ATES is presented byα^{C}, while the fraction of thermal energy reduced by the cooling cycle is 1-α^{C}. α^{C} depends on the temperature of the cold well, operating characteristics of the cooling cycle,

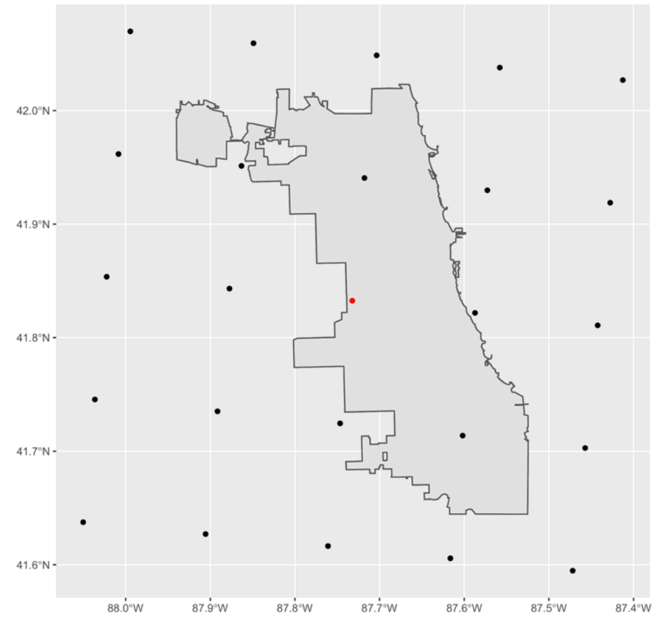

Fig. 4. WRF data grid and Chicago city boundary.

Table 1
Conversion from WRF climate data to EnergyPlus weather data input fields.

EnergyPlus epw file fields	WRF fields	Conversion method
Wind speed (m/s)	wind U and V component at 10 m (m/s)	Compute the norm
Dry bulb temperature (°C)	near surface air temperature at 2 m (K)	No conversion needed
Relative humidity (%)	water vapor mixing ratio at 2 m (kg/kg)	Using methods defined in psychropy.py [61]
Atmospheric pressure (Pa)	surface pressure (Pa)	No conversion needed
Global horizontal radiation (Wh/m^2)	downward short-wave flux at ground surface (W/m^2)	Excel tool developed by Ballarini [60]
Direct normal radiation (Wh/m^2)		
Diffuse horizontal radiation (Wh/m^2)		

and the building energy system. The self-discharge of cold well ($\sigma_{t,s}^{ATES,C}$) is formulated according to Eq. 7B. Finally, electricity consumption used to cool the ATES ($Ref_{t,\,s}^{ATES,C}$) is computed using Eq. 7C. In Eq. 7C, $COP_{t,s}^{Ref,C}$ presents the coefficient of performance of the cooling cycle, which is taken as a function of temperature. The state of the charge of ATES depends on the operating state of the dispatch strategy. Considering State A marked in Fig. 3 (b) the state of the charge of hotwell can be formulated as Eq. (7A).

$$SOC_{t+1,\,s}^{ATES,C} = SOC_{t,\,s}^{ATES,C}\left(1-\sigma_{t,s}^{ATES,C}\right)-\left(Q_{t,s}^{C,B}\alpha^{C}\ -\ Q_{t,s}^{H,B}\alpha^{H}\right)\Big/c^{ATES,C},\ \forall t \in T,\ \forall s \in \Omega,\ SOC_{\min}^{ATES,C} < SOC_{t+1,\,s}^{ATES,C} < c^{ATES,C} \tag{7A}$$

$$\sigma_{t,s}^{ATES,C} = \left(1-\eta^{ATES,Rec}\right)\Big/\Delta t_{Seasonal}^{ATES} \tag{7B}$$

$$Ref_{t,\,s}^{ATES,C} = Q_{t,s}^{C,B}\left(1-\alpha^{C}\right)\Big/COP_{t,s}^{Ref,C}\ \forall t \in T,\ \forall s \in \Omega \tag{7C}$$

- **Thermal recovery efficiency**

In this study, the thermal recovery efficiency of an ATES ($\eta^{ATES,Rec}$) was estimated by a model developed by Bloemendal and Hartog [36]. The model considers the effect of groundwater flow as the primary source of reducing recovery efficiency. When a heated (or cold) fluid of volume V$_{\text{in}}$ is injected into the aquifer of thickness L (assuming the well screened fully across the aquifer), the radius of the hydraulic front R$_{\text{h}}$ from the centerline of the well is given below by considering volume conservation (Eq. (8)).

$$R_h = \sqrt{V_{in}/(n\pi L)} \tag{8}$$

where n is the porosity of the aquifer.

As the injected fluid permeates through the fluid phase of the porous media, the heat stored in the injected fluid dissipates into the solid phase. The absorption of the heat into the solid phase causes the heat front to retard from the hydraulic front, as shown in Fig. 2(a). The radius of the heat front can be evaluated by considering thermal equilibrium (Eq. (9)).

$$R_{th} = \sqrt{\frac{nc_w}{c_{aq}}}R_h \tag{9}$$

where is c_w the volumetric heat capacity of water, c_{aq} is the heat capacity of the aquifer ($c_{aq}\ = nc_w\ + (1\ -n)c_s$), and c_s is the solids volumetric heat capacity.

The impact of ambient groundwater flow on the recovery efficiency is estimated by assuming that a cylindrical shape of the injected volume (the dotted line in Fig. 2(b)) is maintained during the movement of the heated cylinder to the downstream (the solid line in Fig. 2(b)). The displacement distance of the heat source is given by $t_{sp}u^*$, where tsp is the storage period (e.g., half a year) and u^* is the ground water flow rate. When the heat is recovered from the well by extracting a fluid volume equal to the injected volume V$_{\text{in}}$, it is assumed that the heat in the overlap area shown in Fig. 2(b) can be recovered. From the geometry, the overlap area can be computed as follows (Eq. (10)).

$$A_{overlap} = 2R_{th}^2 acos\left(\frac{t_{sp}u^*}{2R_{th}}\right) - t_{sp}u^*\sqrt{R_{th}^2-\frac{1}{4}\left(t_{sp}u^*\right)^2} \tag{10}$$

The recovery efficiency η_{th} is therefore defined by taking the ratio of the overall area $A_{overlap}$ to the original heat source footprint area $A_{footprint}(=\pi R_{th}^2)$, according to Eq. (11).

$$\eta^{ATES,\text{Rec}} = \frac{A_{overlap}}{A_{footprint}} = \frac{2}{\pi}acos\left(\frac{t_{sp}u^*}{2R_{th}}\right) - \frac{t_{sp}u^*}{\pi R_{th}^2}\sqrt{R_{th}^2-\frac{1}{4}\left(t_{sp}u^*\right)^2} \tag{11}$$

The accuracy of η_{th} can be further improved by introducing a coefficient (0.95–0.8) to consider thermal diffusion when there is no groundwater. However, it will be site-specific (aquifer thickness, injection rate and volume, etc). A site-specific numerical simulation should be conducted to determine this up-scaling coefficient for improved optimization analysis. Further details of the model and the discussion on the assumptions is given by Bloemendal and Hartog [36].

The electricity consumption for the thermal loads is formulated by taking the electricity demand for the ATES and the air conditioning demand ($AC_{t,s}$), which cannot be supplied using the ATES according to Eq. (12). In Eq. (12), $\varnothing_{t,s}$ denotes the electricity consumption of the auxiliary devices of the ATES, including the water pumps.

$$E_{t,\,s}^{Th} = HP_{t,\,s}^{ATES,H} + Ref_{t,\,s}^{ATES,C} + AC_{t,s} + \varnothing_{t,s},\ \forall t \in T,\ \forall s \in \Omega \tag{12}$$

SOC model used in this study captures the mass flow including the exchange of mass between the two wells and the water leaks that took place. However, energy has a quality that is not conserved which is described by the Second law of thermodynamics. However, the model has certain limitations in capturing the second law efficiency (in general, most the energy system models used for planning distributed energy systems are not considering the Second Law). The study considers the wells to maintain constant temperature with time (neglecting the temperature drop while the thermal losses take place). Since the Second law

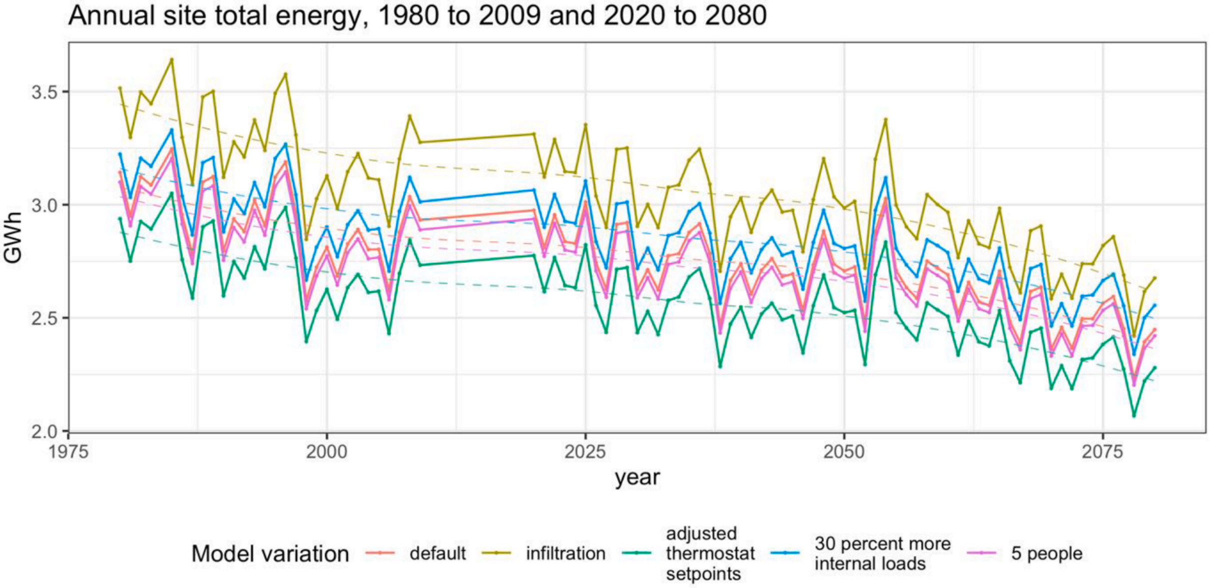

Fig. 5. Annual site energy from 1980 to 2009 and from 2020 to 2080.

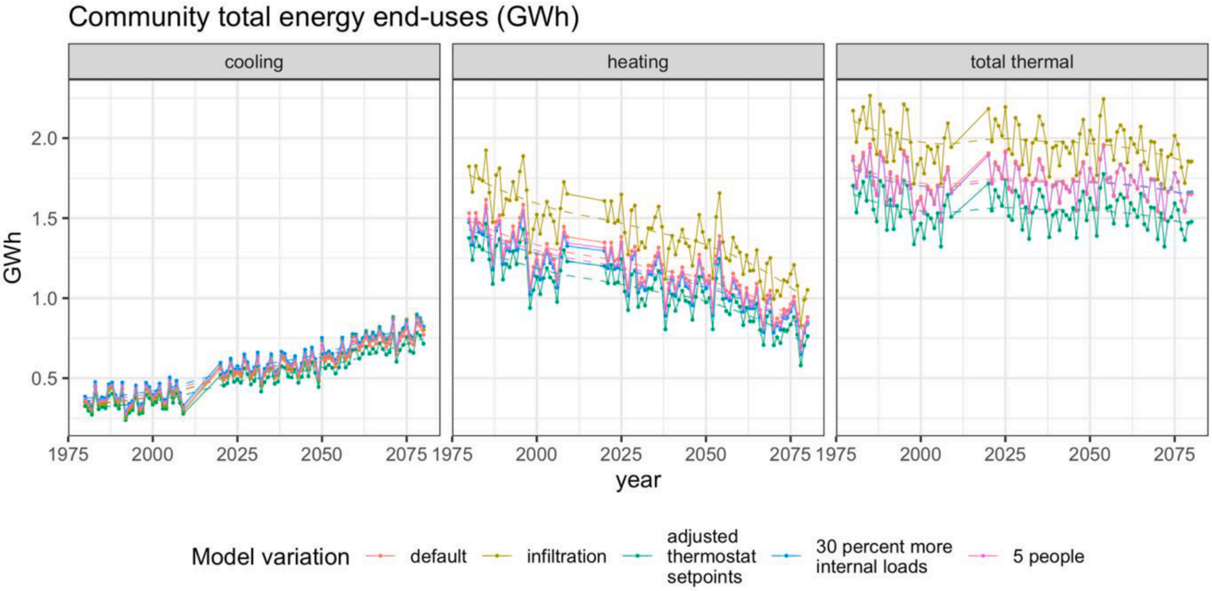

Fig. 6. Annual consumption of main energy end-uses from 1980 to 2009 and from 2020 to 2080.

efficiency (and the thermal losses) may lead to change the temperatures in the wells which we took to be constant, the quality of energy may reduce, leading to poor COP (Coefficient of Performance) in heat pumps. To capture the impact of temperature losses brought by heat transfer, we introduced a coefficient to COP of heat pumps to reflect the practical conditions.

2.3. Dispatch model

The complex formulation of the energy system operation brought up by the ATES with seasonal storage makes it difficult to use a typical linear or mixed integer linear formulation for the dispatch strategy. Therefore, finite and fuzzy state model are used to formulate the dispatch strategy.

2.3.1. Formulation of the dispatch strategy to supply heat and cooling demand

Finite state models are used to formulate the dispatch strategy when supplying the heating and cooling demand, as shown in Fig. 3. The heating demand can be supplied either from the ATES and the assisted heat pump or by using the boiler. The priority is given to use the ATES whenever the hot well can provide the heating demand, since using the boiler will lead to increased carbon dioxide (CO_2) emission levels and add operational costs. Therefore, a boiler is only used to supply the energy demands that cannot be provided by using the ATES. In a similar manner, priority is given to the ATES when supplying the cooling demand. Whenever it is not possible to provide the cooling demand using the cold well, an air conditioner is used. The total electricity consumption due to pumping water or using air-conditioning and heat pumps are summed up to the electricity demand, which is considered in the secondary stage of the dispatch strategy as presented in Ref. [1].

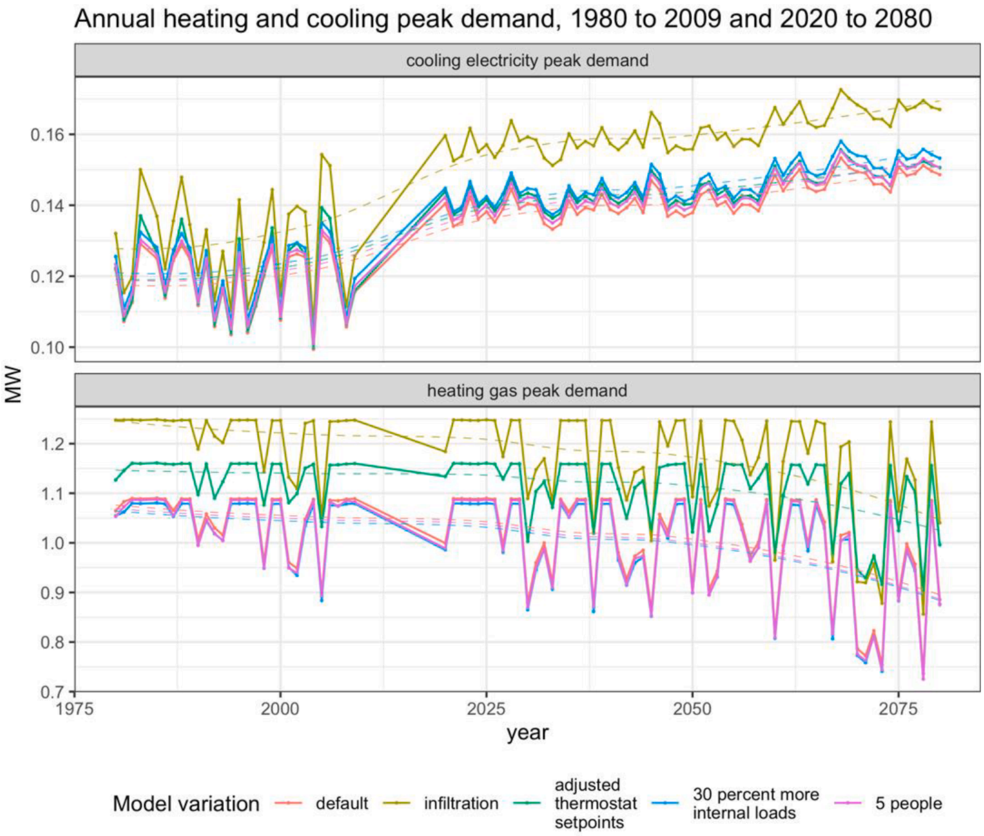

Fig. 7. Annual heating and cooling peak demand of 1980 to 2009 and 2020 to 2080.

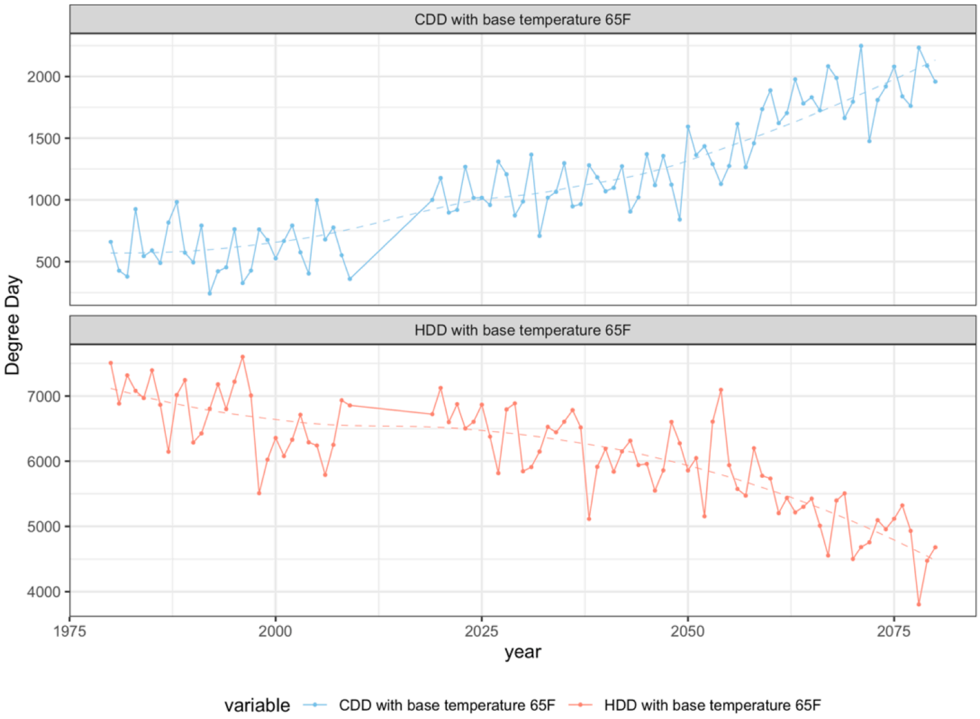

Fig. 8. CDD and HDD from 1980 to 2009 and from 2020 to 2080.

2.3.2. Formulation of the dispatch strategy to provide the electricity demand

The dispatch strategy used for the electricity sector consists of two levels. The first level consists of a fuzzy state model that determines the operating load factor of the diesel generator based on the state of charge level of the battery bank, renewable energy generation, and electricity

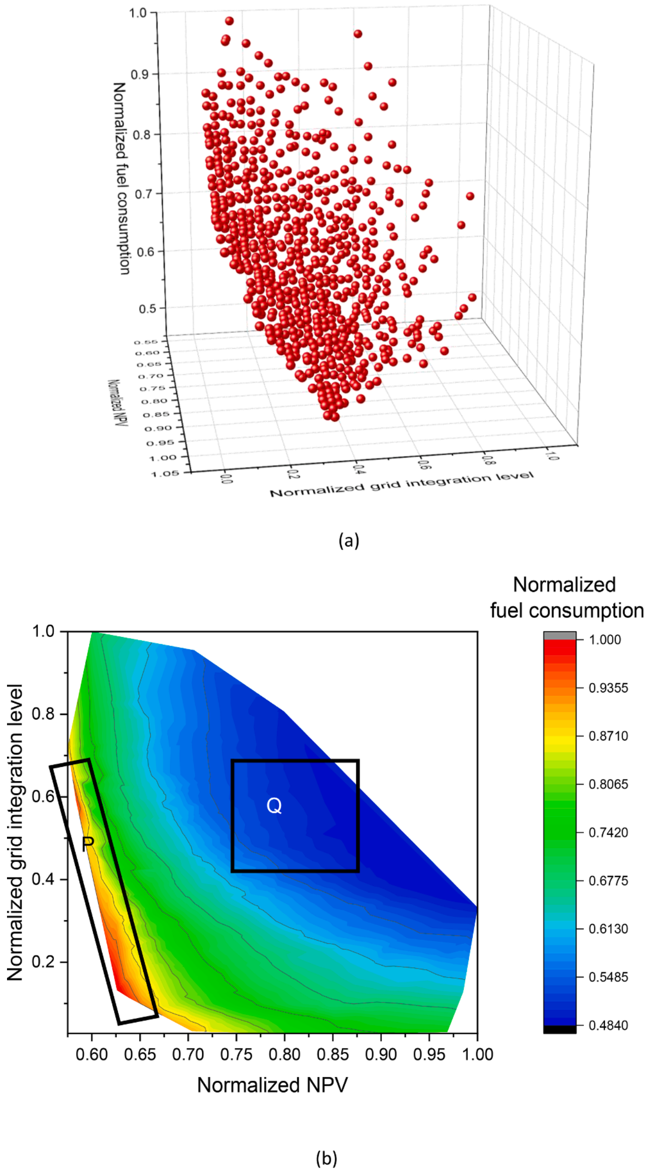

Fig. 9. (a) Scatter plot and (b) contour plot of the Pareto front obtained considering NPV, grid integration level, and fuel consumption as the objective functions. Region P and Q, respectively, present the zones with the highest and lowest fuel consumption.

demand. Fuzzy logic has been used in many applications related to the dispatch optimization of hybrid energy systems [37–40], as it is one of the most promising methods for implementing energy management strategies in hybrid energy systems [41]. After completing the primary level power generation within the energy hub power generation using both renewable energy technologies and ICG can be determined. Further, the mismatch between the energy demand and the power generation also can be computed. The secondary stage of the dispatch strategy is focused on deriving the interactions with energy storage and the electricity grid. Finite state automate is used to derive the operating state of the system in the secondary stage. The mismatch/excess generation within the system, price of electricity in the grid, state of charge in the battery bank, grid curtailments for purchase and injection, and the electricity demand are considered when determining the operating state. An extended explanation of the dispatch strategy can be found in Ref. [42].

2.4. Formulation of objective functions and constraints for optimization

Several performance indicators were used in this study to optimize and analyze the system that is formulated in this section.

2.4.1. Power supply reliability

There will be a breakdown (introduced as loss of power supply, LPS) in the energy supply (including electricity, heating, and cooling) whenever it cannot be provided using the energy hub. For example, loss of power supply in electricity sector ($LPS^{E}_{t,s}$) could take place according to Eq. (13).

$$LPS^{E}_{t,s} = ELD_{t,s} + E^{Th}_{t,s} - P^{RE}_{t,s} - P^{ICG}_{\max} - P^{Bat-Max}_{t,s} - P^{FG-Max}_{t,s}, \forall t \in T, \ \forall s \in \Omega \tag{13}$$

In this equation,$ELD_{t,s}$,$P^{ICG}_{\max}$,$P^{Bat-Max}_{t,s}$, and $P^{FG-Max}_{t,s}$ denote the electricity load demand of the application, nominal power of the ICG, maximum power flow from the battery depending upon the state of charge, and maximum power that can be taken from the grid considering the grid curtailments, respectively. $P^{RE}_{t,s}$ denotes the renewable power generation computed using Eq. (1) and Eq. (2).

The loss of load probability (LOLP) model is used to evaluate the power supply reliability of the energy system in line with Ref. [43] using the loss of power supply. Finally, the expected value of LOLP ($\mathbb{E}(LOLP)_{\forall s \in \Omega}$) is formulated according to Eq. (14), which is used as the performance indicator to evaluate the power supply reliability.

$$\mathbb{E}(LOLP)_{\forall s \in \Omega} = \sum_{\forall s \in \Omega} \psi_s \frac{\sum_{\forall t \in T} LPS^{E}_{t,s} + \gamma^{H} LPS^{H}_{t,s} + \gamma^{C} LPS^{C}_{t,s}}{\sum_{\forall t \in T} P^{ELD}_{t,s} + \gamma^{H} \sum_{\forall t \in T} Q^{H,B}_{t,s} + \gamma^{C} \sum_{\forall t \in T} Q^{C,B}_{t,s}}, \ \forall t \in T, \forall s \in \Omega \tag{14}$$

In this equation, LPS^{H} and LPS^{C} denote loss of heating and cooling demand, respectively. γ^{H} and γ^{C} denote the weighting factor for heat to power and cool to power (the conversion taken as the reciprocal of coefficient of performance of a heat pump and refrigeration cycle [based on the second law of thermodynamics]). ψ_s presents the probability of occurrence for the scenario s ($s \in \Omega$).

2.4.2. Grid integration (GI) level

Grid integration (GI) level presents the autonomy of the distributed energy system, which is considered as an important performance indicator when integrating long-term storage. Higher autonomy is usually expected with the integration of long-term energy storage. Usually, a multi-energy hub could maintain interaction among electricity, thermal and gas grids. However, the present study limited the scope to the interaction between the energy hub and the electricity grid. The GI was defined in number of different ways. The present study used the formulation introduced in Ref. [42], as presented in Eq. (15).

$$\mathbb{E}(GI)_{\forall s \in \Omega} = \sum_{\forall s \in \Omega} \psi_s \frac{\sum_{\forall t \in T} P^{FG}_{t,s}}{\sum_{\forall t \in T} ELD_{t,s}}, \quad \forall t \in T, \forall s \in \Omega \tag{15}$$

P^{FG} and P^{TG} denote the energy units in kilowatt-hours (kWh) purchased and sold to and from the grid during steady state operation in time step t and scenario s.

2.4.3. Net present value

Net present value (NPV) is used in this study as the performance indicator reflecting financial feasibility. NPV has been amply used in the literature to evaluate the financial aspect of energy system implementation projects. In most instances, the formulation of the NPV is simplified by linearizing or by using piecewise linearization methods to fulfill the requirements for the optimization algorithm (especially when conducting stochastic optimization [44–48]); such simplifications were not performed in this study. The NPV consists of initial capital cost (ICC), fixed operation and maintenance cost ($\mathrm{OM}^{\mathrm{fixed}}$), and variable operation and maintenance cost ($\mathrm{OM}^{\mathrm{variable}}$). Cash flows due to the

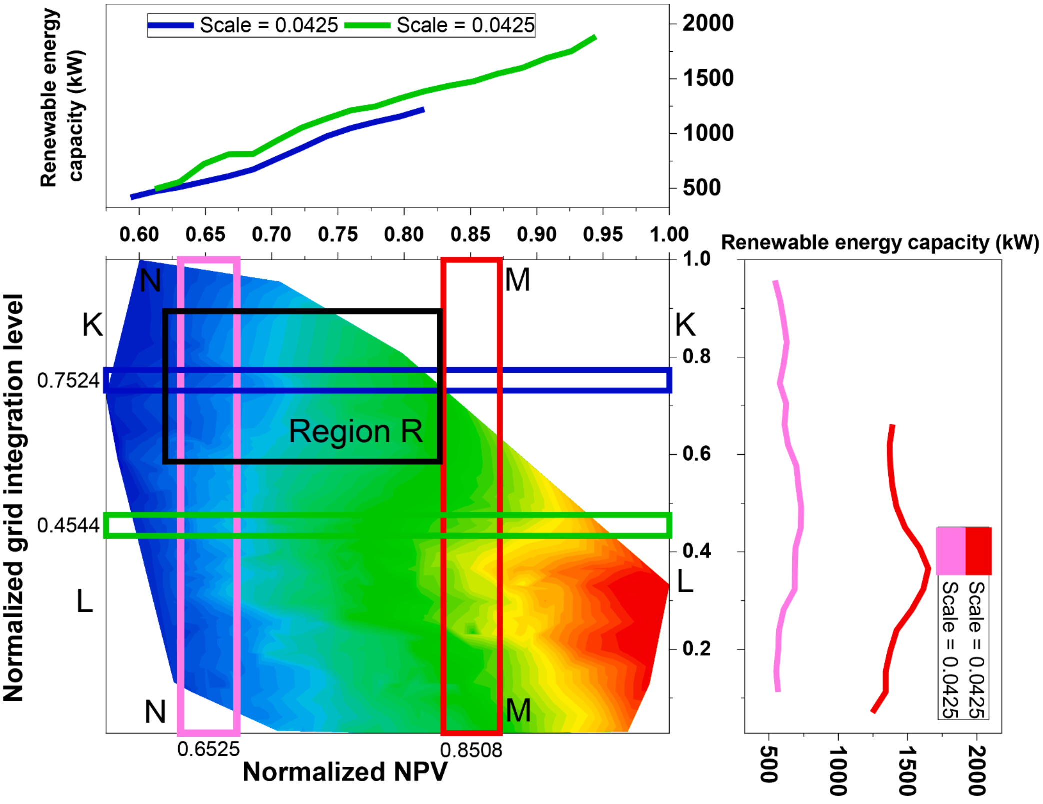

Fig. 10. The contour and sectional plots obtained to assess the variation of renewable energy integration levels of the Pareto solutions.

acquisition and installation of system components are considered under initial capital costs. Cash flows that take place within the lifetime of the project are considered under operation and maintenance cost (OM). Scheduled maintenance, expenses for expenditures such as fuel, or income from grid interactions and other factors are considered under OM^{fixed}. $OM^{variable}$ considers the cost components related to replacement of system components such as battery banks, inverters, and ICG. The operation and maintenance cost (OM) is computed using Eq. (16).

$$OM_s = \sum_{\forall c\in C}\left(OM^{Fixed}_{c,s}\,CRF_c\right) + \sum_{\forall h\in H}\sum_{\forall c\in C} PRI^{l} OM^{variable}_{c,h,s}, \quad \forall s\in\Omega, \forall c\in C, \forall h \in H \tag{16}$$

In this equation, CRF_c denotes the capital recovery factor for the c^{th} component. PRI denotes the real interest rate calculated using both interest rates for investment and the local market annual inflation ratio. The year is presented by h.

Finally, the levelized energy cost (LEC) of all the cash flows is calculated combining initial capital cost (ICC) and OM according to Eq. (17).

$$\mathbb{E}(\mathrm{LEC}) = \sum_{\forall s\in\Omega}\psi_s \frac{\mathrm{OM}_s + \mathrm{ICC}}{\sum_{\forall t\in T} P^{ELD}_{t,s} + \gamma^{H}\sum_{\forall t\in T} Q^{H,B}_{t,s} + \gamma^{C}\sum_{\forall t\in T} Q^{C,B}_{t,s}}, \quad \forall t\in T, \forall s\in\Omega \tag{17}$$

2.4.4. *Flexibility of the system*

The flexibility has been defined in number of different ways, considering the aspects of demand, generation, transmission, and distribution [49]. Although flexibility has been defined as operation of the system, Kondziella and Bruckner [50] highlighted the importance of enhancing the flexibility at the early design stage, which is quite vital. Perera et al. [51] redefined the flexibility concept, focusing on the design aspect of distributed energy systems addressing this bottleneck being linked to the stochastic optimization of distributed energy systems. In this model, *flexibility* is defined as considering all the criteria related to evaluate the system, including LEC, reliability, renewable energy utilization, and CO_2 emissions based on the flexibility concept practiced in manufacturing systems [52,53]. In this model, performance change in each criterion due to the changes in the external factors is calculated first. *Flexibility* is defined for the Pareto solutions obtained from the multi-objective optimization by using the scenarios used for the stochastic optimization. Performance degradation for criterion n (PD_n) is calculated according to Eq. (18) with respect to a reference scenario. In this study, the expected values for the performance indicators (which enables to consider all the scenarios) is used as the reference value ($CI_{D,n}$). The deviation of the each performance indicator for each scenario with respect to the reference value is considered when computing the flexibility. Higher flexibility will lead to minimize the deviation.

$$PD_n = \sum_{\forall s\in\Omega}\psi_s\left(CI_{s,n} - CI_{D,n}\right)\Big/ CI_{D,n} \tag{18}$$

Relative change due to the changes that take place in the system input is taken the measure to evaluate the flexibility. Coefficient of closure (CC) defined in the Technique for Order of Preference by Similarity to Ideal Solution (TOPSIS) is used to evaluate the flexibility of design solutions. A comprehensive explanation about the method is presented in Ref. [51].

2.5. *Optimization algorithm and high-performance computing (HPC) implementation*

System sizing of distributed energy systems has been widely discussed in recent literature. Refs. [54,55] provide a review on the present state of the art. However, stochastic optimization of long-term energy storage has not been discussed widely, since it is quite challenging to perform such optimization. The study present relates with longterm energy storage and investigates the impact of future climate variations where lengthy time series are required to be considered for each

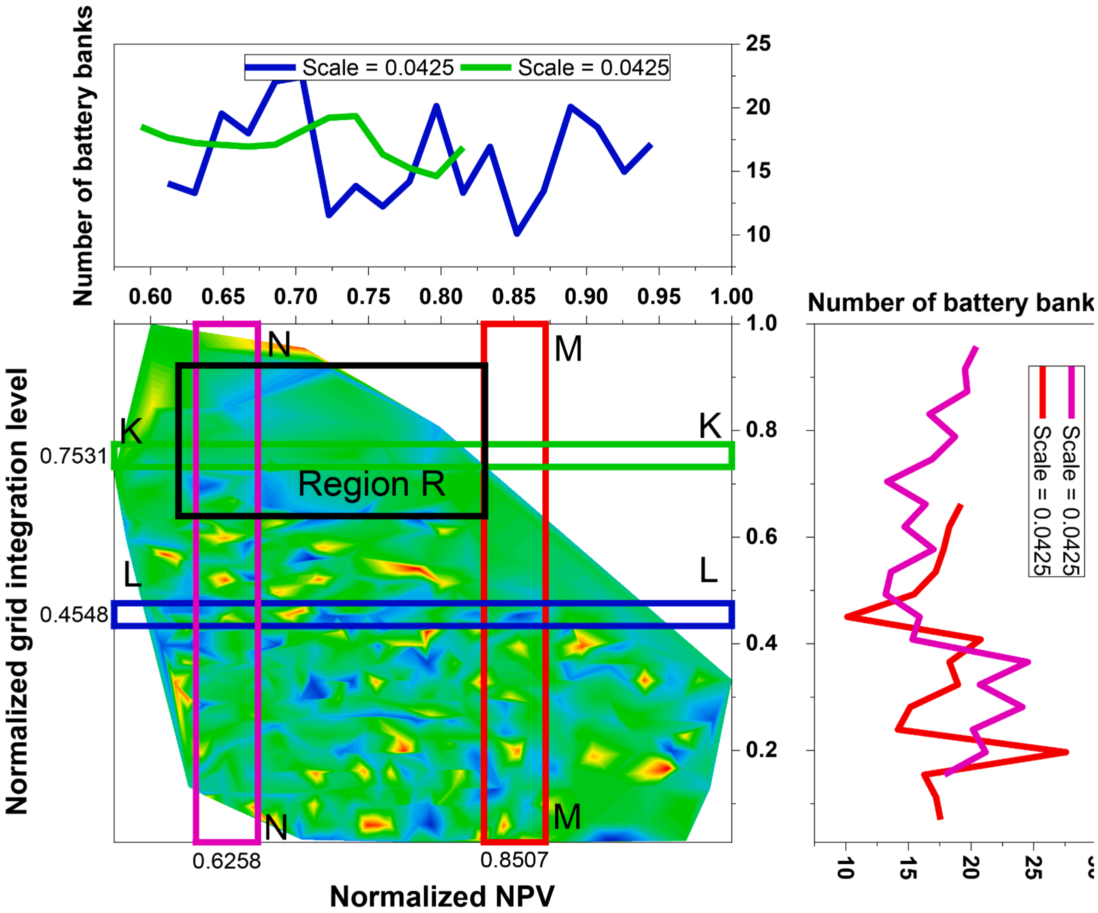

Fig. 11. The contour and sectional plots obtained to assess the variation of energy storage size of the Pareto solutions.

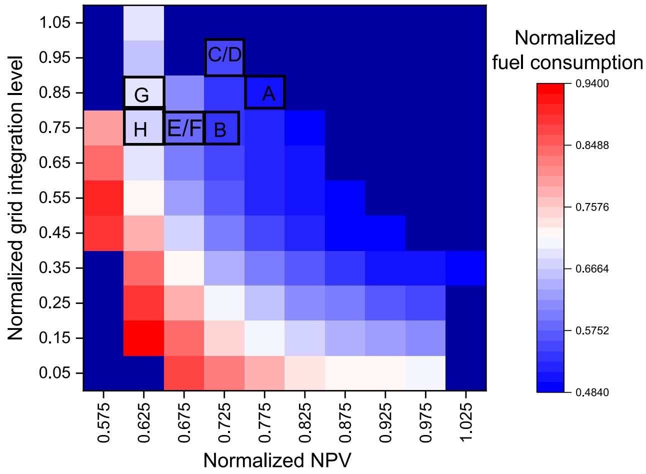

Fig. 12. The heat map of the Pareto front (having ATES design solutions) with seven design solutions marked within the heat map. See Table 2 for a detailed system configuration of these designs.

scenario. The stochastic optimization which used to be conder a pool of scenarios results in a large pool of decision space variables which makes it quite challenging to handle. In addition, the geothermal model used with ATES further complicates the optimization process. This can be understood when referring to the recent work on stochastic optimization where LP with Dantzig–Wolfe decomposition [2]. Ref. [2] end up in difficult situation to handle the optimization problem (even with a short time series which is not sufficient to evaluate the impact brought up by the future climate variations).The typical LP/MILP approach uses a value based approach when solving the dispatch problem where the huristic method used in the present study uses a policy based approach when solving the dispatch problem. The decision space notably reduce when using a policy based approach which makes it possible to hangle the complexity of the problem with the support of High Performance GPU computing. Therefore, a heuristic approach was used in the present study. Heuristic algorithms such as particle swarm, simulated annealing, and evolutionary algorithms are used to optimize distributed energy hubs due to the complexity of the objective functions [56].

Heuristic algorithms demand extended computational time for optimization. Therefore, performing stochastic optimization with objective functions formulated using an extended period of simulation can be an exhaustive task. To address this bottleneck, the present study used graphical processing unit (GPU) accelerated computing. The modern GPUs are a collection of thousands of simple central processing units (CPU) that can perform independently. As a result, they enable large-scale parallelization, greatly reducing the computational time. This enables researchers to perform stochastic optimization with a large pool of scenarios, including stochastic optimization based on evolutionary algorithms [57,58]. The computational algorithm consists of two components. The first is used for the simulation-based evaluation of objective functions, which is implemented in the GPU. The second is devoted to the elements of the optimization algorithm that are implemented in the CPU. The decision space of the energy system optimization problem consists of design parameters of the energy hub and dispatch strategy. The parameters of the system design include the following:

Table 2
Selected design solutions with ATES extracted from the Pareto front.

Sys.	NPV[1]	GI[2]	FC[3]	TG[4]	REC[5]	SPV[6]	BB[7]	ICG[8]	Flex[9]	ICG[10]	ATES[11]
A	7.33	14.56	0.45	92,240	1165	77.7	23	40	61.3	3199	1500
B	7.03	12.54	0.47	79,415	1125	64.4	21	40	57.5	2759	1250
C	6.63	16.52	0.49	104,643	815	85.3	22	40	57.5	4690	1250
D	6.48	17.22	0.50	109,096	695	91.4	21	40	53.8	6382	1000
E	6.14	14.31	0.53	90,641	700	68.6	21	40	52.7	4706	1000
F	6.10	12.94	0.54	81,983	665	66.9	23	40	50.4	3471	500
G	5.91	14.87	0.56	94,201	535	77.6	22	40	47.8	4100	500
H	5.47	11.28	0.68	71,448	460	56.5	14	40	46.2	17,354	250

[1] Net present value (x $1,000,000).
[2] Grid integration level (%).
[3] Fuel consumption (x1,000) in litres.
[4] Energy injected to the grid (kWh).
[5] Installed renewable energy capacity (kW).
[6] Percentage of solar PV in installed renewable capacity.
[7] Number of battery banks.
[8] ICG capacity (kWh).
[9] Flexibility.
[10] Power generation from the ICG (kWh).
[11] ATES capacity injection/production rate m^3/day.

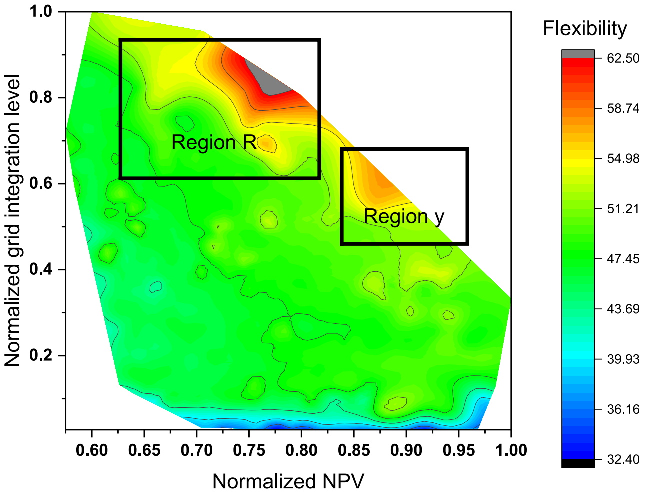

Fig. 17. Contour plot presenting the flexibility of Pareto design solutions. Flexibility levels are substantial considering lower grid integration levels. Higher flexibility is demonstrated by design solutions within Region R with ATES.

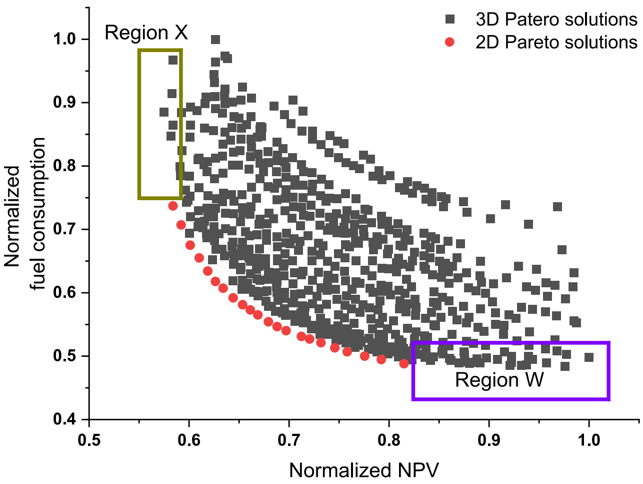

Fig. 18. A 2D Pareto front obtained with ATES in the decision space considering fuel consumption and NPV as objective functions. Region W and X represent the design solutions with lowest fuel consumption and cost, which are not captured by the 2D Pareto front.

- Type and capacity of the wind turbines and SPV panels, which represent renewable energy components.
- ICG, ATES, and battery bank capacities, which represent dispatchable sources and energy storage (both thermal and electricity).

The parameters related to the dispatch strategy include:

- weight matrix, which represents fuzzy logic rules for the secondary level dispatch strategy for electricity, and
- state transition points for the secondary level dispatch strategy for electricity.

The net present value of the system, grid integration level, and fuel consumption are used as the objective functions. Loss of load probability is considered to be a constraint for the optimization.

A number of optimization techniques have been used to minimize the difficulties brought up by the uncertainties brought up by future climate variations and the building energy usage. Techniques such as stochastic, robust and stochastic-robust techniques have been used in this context. The robust optimization is computationally less intensive. However, it often lead to a more conservative design. In contrast, stochastic optimization is computationally intensive but leads to a more realistic energy system design. Designing distributed energy systems (capacity sizing) is more challenging hence it leads to a coupled optimization of dispatch and system sizing. In order to address these difficulties, sample average approximation method [1] is used this study to perform stochastic optimization. It has been used in the present state of the art energy system optimization by Sharafi and El Mekkawy [2] and Perera et al [3] for simulation-based optimization to optimize standalone energy systems. However, none of these studies have considered the thermal energy storage or long term energy storage. A Steady ε-State Evolutionary Algorithm [59], based on the ε-dominance technique, was accordingly used in this study to conduct the optimization process. A comprehensive overview about the optimization algorithm and implementation of the dispatch strategy can be found in Refs. [23,42].

3. Case study

3.1. Description about the district of buildings

To acquire a community-level load profile, a stochastic model is used

Table A1
Cost values for the system components.

Component	Description	Cost($)
Wind Turbine (12 m) (20 year life time)	5 kW	6000
	10 kW	9000
Solar Panels (20 year life time)	(variation plotted below (Fig. A1-1))	(variation plotted below (Fig. A1-1))
ICG	0.5kVA – 7.5 kVA (single phase) (20000 working hours)	335.5–2195
ATES	Considering 1000 m3/day injection or production (the cost is assumed to vary linearly with the injection or production)	215,112
	Hourly O&M	0.16/kW
Cost of fuel	(Diesel 1 L)	0.8
Battery	12 V, 250Ah	380
Inverter	Single phase up to 50 kW (four years lifetime)	400–700
Heat pump (ASHP)	300 kW linear variation is assumed	7.95
Cogeneration	300 kW (Max.) A linear variation is assumed	115/kW
Solar thermal	(variation plotted below) Capture area(CA) 50 m^2 for water heating	$4777.4x\ (CA)0^{.421}$

Table A2
Basic parameters of cost model used for Chapter 2, 5 and 10. Eurostat [3] is used to convert the cost data for other European cities corresponding to other chapters.

Parameter	Fraction (%)
SPV Panel & Wind Turbines	
Installation cost as a fraction of acquisition cost	15
Annual O&M as a fraction of acquisition cost	2
ICG Installation cost as a fraction of acquisition cost	5
Local market annual inflation rate	2
Return on Investment	6

to combine the scaled-up simulation results of one single-family home model with five different configurations and 90 years of different weather data in the city of Chicago.

The single-family prototype model was developed by Pacific Northwest National Laboratory (PNNL) and complied with the International Energy Conservation Code (IECC) 2006 standards. It is a two-story detached house with a conditioned floor area of 220 square meters (m^2) and an unconditioned attic of 110 m^2. The HVAC system is a typical residential split system with a single-speed direct expansion cooling coil and a gas heating coil. To account for the variability of the district loads, five variations of the model were introduced to produce five load profiles of the district:

- Defaults: the default settings that comply with the requirements of IECC 2006 standards.
- Infiltration: This variation had a 30% higher zone infiltration, where the ZoneInfiltration:EffectiveLeakageArea object, used in EnergyPlus to describe infiltration, was set to 1,240 square centimeters (cm^2) instead of 953 cm^2, as in the default setting.
- Thermostat setpoint: This variation had a 2 °C higher cooling setpoint and a 2 °C lower heating setpoint before 7 am and after 10 pm to represent thermostat reset during sleep time, compared with the default settings.
- Occupancy: The number of occupants in this variation was increased to five from three in the default setting.

Table A3
Parameter values of the geothermal model.

Parameter	Value	Unit	Description
tcycle	365	day	seasonal storage, cycle duration
tsp	92	day	seasonal storage, injection/production duration
Q	1000	m^3/day	
L	50	M	aquifer thickness
u^*	0.1	m/day	groundwater velocity
n	0.3		aquifer porosity
porcap	0.1		cap/bed porosity
Cw	4.18E + 06	J/(m^3 K)	water heat capacity
Cs	2.60E + 06	J/(m^3 K)	solids volumetric heat capacity
Caq	3.08E + 06	J/(m^3 K)	aquifer heat capacity
Ccap	2.76E + 06	J/(m^3 K)	cap/bed heat capacity

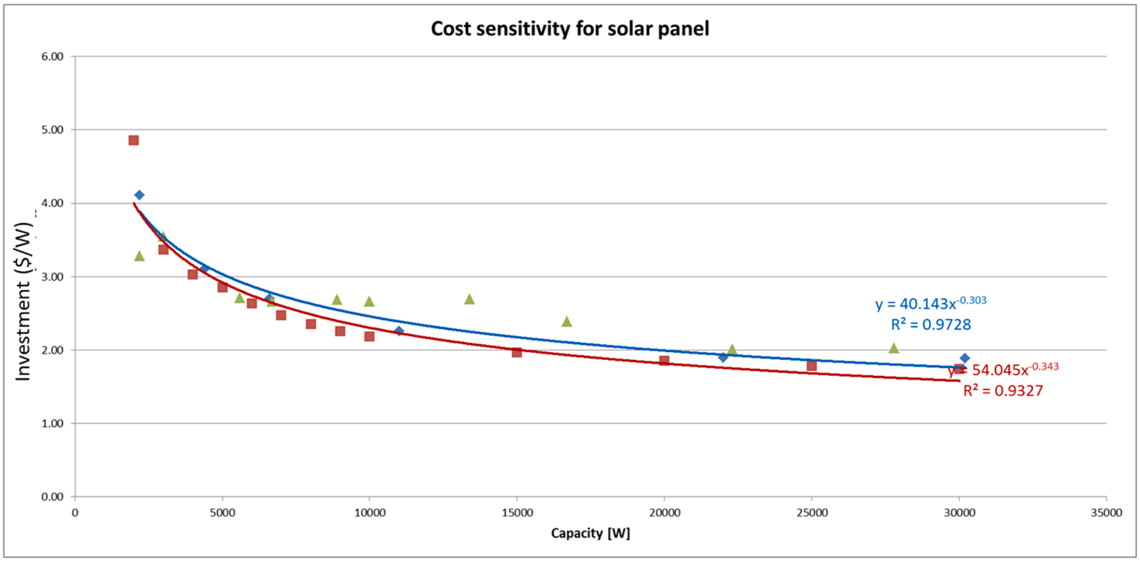

Fig. A1. The variation of Solar PV Cost with the capacity installed considered for the study.

- Internal loads: This variation assumes 30% higher internal loads; the lighting power density was changed from 2.06 to 2.62 W per square meter (W/m^2).

The simulation uses 90 years' weather data during 1980–2009 and 2020–2080 for a location close to O'Hare International Airport.

Five community-level load profiles were generated by scaling up the energy and demand outputs of each of the five variations of the prototype house model by 58. The multiplier was determined to ensure the highest hourly peak thermal load of any of the five scaled load profiles would not exceed 1 MW.

3.2. Curation of climate data

The historic climate data of 1980–2009 and future climate data of 2020–2080 for scenario RCP8.5 was retrieved from model output of the Weather Research and Forecasting (WRF) model, version 4.2.1. The data are gridded at 12 km (km)-by-12 km resolution, downloaded from the Globus endpoints.[1] Fig. 4 shows the weather data grid and the city boundary of Chicago. The weather data at the red grid point was selected to represent the city, due to its proximity to the center of the city, (41.8781°N, 87.9090°W).

Six variables were downloaded: (1) near surface air temperature at 2 m, (2) wind U component (the east-going component of the horizontal wind), (3) the V wind component (the north-going component of the horizontal wind) at 10 m, (4) the water vapor mixing ratio at 2 m, (5) surface pressure, and (6) downward short-wave flux at ground surface. These variables were converted into six EnergyPlus weather file input fields: dry bulb temperature, relative humidity, atmospheric pressure, global horizontal radiation, direct normal radiation, and diffuse horizontal radiation. The downward short-wave solar irradiance at ground surface was separated into the three solar radiation inputs in the EnergyPlus weather file using the Excel tool developed by Ballarini [60]. The wind speed was derived from the wind U and V components. Relative humidity was computed from dry bulb temperature, ambient pressure, and humidity ratio using functions defined in psychropy.py [61]. Table 1 shows the conversion.

3.3. Assessment of the energy demand

This section summarizes the distribution of the annual total site energy, energy end uses, and peak demand of the residential community, across five different model variations over 90 years. From 1980 to 2080, the annual total site energy gradually decreased for all five model variations described in Section 3.1 Fig. 5. Fig. 6 shows the annual energy end uses of the community over time. We can see a slight increase in cooling energy use and a decrease in heating energy use. This agrees with the increase in cooling degree days (CDD) and a decrease in heating degree days (HDD) from 1980 to 2080. The overall site energy use and total thermal energy consumption decreased, as the climate in Chicago is heating dominant. The equipment and lighting energy stayed the same over time. For the cooling end use, the model with 30% more internal loads had the highest consumption across all years, and the model that adjusted thermostat setpoints had the lowest consumption over time. The cooling consumption of the other three model variations were in between, with the default model slightly lower than the other two. For heating and total thermal (the total of heating and cooling) end use, the model with increased infiltration had the highest consumption, and the model that adjusted thermostat setpoints had the lowest consumption. For lighting and equipment, the model with 30% more internal loads had the highest consumption, while the other four model variations had the same consumption in these two end uses.

In Fig. 7, the plot of cooling and heating peak demand reveals a slight increase in cooling electricity peak demand and a decrease in heating gas peak demand over the years. This also aligns with the trend of increased CDD and decreased HDD over time, as shown in Fig. 7. The model variation with increased infiltration had the highest electricity and gas peak demand.

Fig. 8 shows the annual HDD and CDD from 1980 to 2009 and from 2020 to 2080. The CDD doubled and the HDD decreased by a third from 1980 to 2080. This climate change pattern agrees with the trend of increased cooling and decreased heating consumption and peak demand shown in Fig. 5 through Fig. 7. Some leveling-off behavior is observed in the heating peak demand in Fig. 7, due to equipment under-sizing using the ASHRAE design day. The ASHRAE design day assumes a −20 °C temperature throughout the day. However, for some of the years, like 2024, there is a day with outdoor air temperature below −20 °C throughout the day, with a minimum of under −30 °C. Even with global climate change, there could still be very cold days. The frequency of those days might reduce, which corresponds to the reduced frequency of the leveling-off of the peak heating demand.

3.4. Scenarios for the stochastic optimization

The variation of energy demand discussed in this section which was brought up by future climate variations as well as model variations were taken as the basis for the stochastic optimization. The future climate variations are having an impact into the renewable energy generation in addition to the energy demand which was captured in the energy system optimization. The demand and renewable energy potential for the future climate conditions obtained from 2020 to 2080 for scenario RCP8.5 from Weather Research and Forecasting (WRF) model was the basis for the scenarios generated (the past recoded data are not considered). 60 scenarios are generated taking each year as a separate scenario (each time series consist of 8760 timesteps 24x365) which will have a unique energy demand, wind speed and solar irradiation data. Subsequently, the impact of demand uncertainty is further investigated by extending the scenario tree. The uncertainty brought up by infiltration, adjusted thermostat setpoints, changes of internal loads and changes in occupancy were considered by adding an additional scenario leading the pool of scenarios up to 300. The impact of these 300 scenarios on the energy system is considered during the optimization which presents the impact of uncertainties brought up by human and climate systems.

4. Results and discussion

A techno-economic assessment was performed to assess the feasibility of distributed energy systems with ATES. The possibility of using ATES to improve energy autonomy, as well as to support less dependence on fossil fuels, are evaluated in this section. Less dependency on fossil fuels implies less dependency on their associated CO_2 emissions (eco-friendliness).

4.1. Cost-fuel consumption and grid integration Pareto front

A Pareto optimization was performed considering net present value, fuel consumption, and grid integration level. Fossil fuel consumption is a reflection of the CO_2 emissions by the system, which does not include the CO_2 impact of grid electricity (in this case it is not in favor of ATES, since the CO_2 levels in the grid electricity are reasonably high). A well distributed Pareto front is observed in Fig. 9 (a) when considering these three objectives. Each design solution represents a unique system design with a unique operational strategy. The well distributed Pareto front (Fig. 9 (a)) demonstrates that these three objectives are conflicting among themselves. As a result, it is not possible to maximize these performance indicators simultaneously. A 2D contour plot of the Pareto front was obtained to get a more detailed overview of the Pareto front (Fig. 9(b)). Region P in Fig. 9 (b) presents the design solutions having a

---

[1] https://app.globus.org/file-manager?origin_id=c296b088-b769-11eb-afd8-e1e7a67e00c1&origin_path=%2F.

highest fuel consumption, which tends to distribute in a very small portion of the Pareto front, where NPV is quite low. The design solutions having the lowest grid interaction levels show relatively lower fuel consumption when compared to those in Region P. Region Q presents the design solutions with the lowest fuel consumption, which is well distributed, taking a reasonably large portion of the contour plot. A sharp reduction in fuel consumption is observed from region P to region Q when the grid integration levels are between 0.4 and 0.6 (also noticeable in the scatter plot). Boilers and ICG play a major role in Region P compared to the design solutions in Region Q.

It is important to assess the changes in system design when varying the performance indicators throughout the Pareto front. The renewable energy capacity (the sum of both PV and wind installed) and energy storage capacity for the Pareto solutions were assessed, respectively. A contour plot of normalized NPV, normalized grid integration level, and installed renewable energy capacity was created, and four cross sections taken with constant normalized NPV and grid integration levels (Fig. 10). The contour plot clearly demonstrates that the installed renewable energy capacity shows a clear pattern when moving from the design solutions with lower NPV to higher NPV. This could be understood further by looking into cross section L-L, which was taken (2d cross section taken from the full 3d results space and displayed for simplicity sake) with a fixed normalized grid integration level. The renewable penetration level increased with the increase of NPV. When moving from L-L to K-K, a similar variation in renewable energy capacity can be observed. However, in K-K, the gradient is slightly lower than the L-L. In contrast, both N-N and M−M do not show a significant variation in the installed renewable energy capacity (except a small portion in MM). A significant variation in the renewable energy capacity takes place within Region R. Therefore, design solutions with a wider capacity of renewable energy technologies can be observed in this region.

The size of the battery storage of the Pareto solutions obtained do not reflect a clear pattern, as shown in the contour plot in Fig. 11 being different from the renewable energy capacity. The two cross sections T-T and S-S were taken from the contour plot with constant NPV. A complex variation in energy storage size is observed when increasing the grid integration level. It varies from 10 to 28 when moving across the contour plot. Similarly, the cross-section V-V taken with constant grid integration level shows a complex variation in the storage size. However, the storage size is more stable in the cross-section U-U, especially within Region R. Therefore, in contrast to the renewable energy capacity, more stability is observed within Region R concerning energy storage.

4.2. Role of ATES in distributed energy systems

It is interesting to assess the role of ATES within the energy system. Although we observe a well distributed Pareto front with a large pool of alternative solutions, designs with ATES are limited to a small portion in the Pareto front (only limited to Region R). Region R includes design solutions with a higher grid integration level and relatively low NPV. A heat map of the 3D Pareto surface was taken, and Pareto solutions with ATES were taken from different sections of Region R to further assess the impact of ATES on performance indicators and the renewable energy integration process (Fig. 12). Accordingly, seven design solutions representing six zones within Region R were taken and tabulated in Table 2.

The ATES capacity has a clear impact on the performance indicators, as well as the system design (especially renewable energy integration). The design solution with higher ATES capacity tends to consume less fuel and demonstrate the potential to integrate more PV and wind energy (Table 2). For example, when moving from System A to D, and subsequently H, the installed renewable energy capacity reduces from 1,165 to 695 and 460 kW. The direct impact of reduction in installed renewable energy capacity is reflected in the heat map. Renewable energy integration drops notably when reducing the capacity of the ATES. The renewable energy capacity increases linearly with the size of ATES demonstrating the potential of ATES technology to enhance the renewable energy penetration levels. In a similar manner, the cost increases as we increase the capacity of ATES The NPV is increasing from 5.47 to 7.33 $\times 10^6$ \$ when moving from system H to A. As a result, ATES can not be observed in the cost optimal designsolutions. This clearly indicate the economic challengues that need to be faced when popularizing the ATES technology. It is expected that the technology maturity willaddress this bottleneck in the future.

The ICG capacity increases, respectively, from 3,199 to 6,382 and 17,354 kWh. System A lays at the edge of the Pareto front with a very low fuel consumption rate of 4500 L per year which increases upto 6800 when moving into H. As discussed in the previous section, the size of the battery storage does not change notably, except for System H. Similarly, the ICG capacity stays constant, and the power generation from the ICG does not vary significantly (except with systems H and D). Similarly, the grid injection of excess power generated does not show a significant change among the design solutions. For example, systems C and D inject over 100 megawatt-hours, which accounts for about 16% of the total energy demand of the building stock (after converting the thermal load into the electricity demand). It can be concluded that higher ATES capacity will lead to an increase in the installed renewable energy capacity while reducing the fuel consumption. A slight increase in the grid integration level is observed which assists the renewable energy integration being the buffer. Therefore, ATES is an ideal way to improve the renewable energy penetration level and minimize the dependence on fossil fuels with reasonable support from the grid (to assist the fluctuations in both demand and generation).

4.3. Overall assessment of ATES integration

Following the detailed assessment conducted at the system component level, a more holistic assessment considering the performance indicators was performed. The main performance indicators to be considered in this context were flexibility, cost, and fuel consumption. To achieve this objective, flexibility levels of the Pareto solutions were plotted in the contour plot in Fig. 5. Flexibility is a broad concept and can be defined in a number of ways. However, quantifying the flexibility of a system at the early design stage is a challenging task. In this study, we used the definition presented by Perera et al. [51] to quantify flexibility. According to Perera et al. [51], a system with higher flexibility should not show a significant deviation in its performance indicators due to the changes brought by the external factors. In this specific case, the changes brought by future climate variations on demand and renewable energy potential were taken into consideration when assessing flexibility. As shown in Fig. 17, design solutions with the lowest grid integration level (which operates in stand-alone mode) had the lowest flexibility levels. These designs need to withstand the fluctuations brought by external sources without any external support, which leads to a poor flexibility level. On the other hand, designs belonging to Region R had the highest flexibility levels. This clearly indicates that ATES can notably improve the flexibility levels of the distributed energy system. The most important fact is that higher flexibility is achieved with a reasonably high renewable integration level. For example, System A (with the highest ATES capacity) in Table 2 had the highest renewable energy integration level, while at the same time having the highest flexibility level. However, Region Y in Fig. 17 presents a zone with higher flexibility without ATES. The energy systems in Region Y are having lower grid interaction when compared to Region R. The design solutiuons in Region Y consists of higher renewable energy penetration levels and a larger battery storage. A higher waste of renewable energy (renewable energy that can not be utilized) is observed in this region. Due to the larger capacity of battery ban and the renewable energy that can not be utilized the the NPV is notably high in Region Y when compared to Region R. This clearly reflects the contribution of ATES in improving flexibility while supporting renewable energy integration.

It is clear that ATES has a positive impact on flexibility and renewable energy integration levels. However, ATES also depends on the grid considerably, which leads to a reduced autonomy level of the distributed system (discussed earlier). In order to understand the impact of ATES on the NPV and fuel consumption, a 2D Pareto optimization was performed with ATES in the decision space and compared with the 3D Pareto solutions obtained previously (Fig. 18). It is clearly reflected that the Pareto solutions of the 3D Pareto front merge with the Pareto solutions of 2D Pareto front when considering the alternative design solutions with lowest NPV and fuel consumption. However, the 3D Pareto front provides alternative designs with lowest fuel consumption and net present value, as shown in Regions W and X, which are not covered by ATES. Therefore, ATES does not emerge as the optimal alternative design, although it has many merits when used to simply conduct a cost optimization. We believe that the technology maturity of ATES will improve to address these limitations, and it will become a leading component in distributed energy systems due to its potential to improve flexibility and renewable energy integration levels.

5. Conclusions

Energy storage has been widely discussed in the recent past and is known to be a major driver in the fight against climate change. Among energy storage technologies, long-term storage has gained much attention due to its potential to enhance renewable energy penetration levels notably. More important, long-term storage could play a vital role when enhancing the climate resilience of energy infrastructure. However, design optimization of distributed energy systems with long-term energy storage that account for future climate variations is a challenging task, since stochastic optimization of such energy systems presents a number of challenges.

The present study has successfully addressed these bottlenecks and developed a stochastic optimization model to design multi-energy systems, including electrical and thermal storage (long term). Furthermore, to the best of authors' knowledge, it is the first study that performed design optimization of a distributed energy system that includes aquifer thermal energy storage (ATES). Although techno-economic assessment has been performed for ATES in the present state of the art, its potential to be a part of distributed energy systems has not been widely discussed. The complex energy flows and the impact of geotechnical phenomena on energy storage heighten the challenge of including ATES into the energy system optimization process. This study reveals that ATES has the potential to facilitate renewable energy integration while maintaining flexibility, rather than relying on an internal combustion generator or a battery bank. Furthermore, ATES works in harmony with the battery bank, which enables the energy system to be flexible by using both short-term and long-term storage. Furthermore, ATES demonstrates the potential to notably reduce fuel consumption. These unique features will support the energy transition by helping to decarbonizing the building sector. Note, however, that ATES does not become either the lowest cost or lowest fuel consumption solution, even with the stochastic model. A price reduction of ATES technology is needed for that to occur; however, that can be expected as the technology matures.

6. Data availability

The data relevant to the energy and geothermal not found in the manuscript are available from the corresponding author upon reasonable request.

Declaration of Competing Interest

The authors declare that they have no known competing financial interests or personal relationships that could have appeared to influence the work reported in this paper.

Data availability

Data will be made available on request.

Acknowledgements

This work was supported by Lawrence Berkeley National Laboratory (LBNL) with funding from the Geothermal Technologies Office and under Department of Energy Contract No. DE-AC02-05CH11231.

Appendix A

This section includes the supporting data for the model used. Table A1 presents the cost values used in the model while Table A2 presents the parameters used for the cost model. Fig. A1 presents the variation of solar PV cost with the capacity installed. Finally, Table A3 presents the parameter values of the geothermal model.

References

[1] IPCC Fifth Assessment Synthesis Report. IPCC 5th Assessment Synthesis Report n.d. http://ar5-syr.ipcc.ch/ (accessed May 25, 2018).
[2] Photovoltaic made in China | REVE News of the wind sector in Spain and in the world n.d. https://www.evwind.es/2022/09/24/photovoltaic-made-in-china/87989 (accessed October 10, 2022).
[3] China Installed Record Amount of Rooftop Solar in 2021. BloombergCom 2022.
[4] Will system integration of renewables be a major challenge by 2023? – Analysis. IEA n.d. https://www.iea.org/articles/will-system-integration-of-renewables-be-a-major-challenge-by-2023 (accessed September 7, 2022).
[5] Ibrahim H, Ilinca A, Perron J. Energy storage systems—characteristics and comparisons. Renew Sustain Energy Rev 2008;12:1221–50. https://doi.org/10.1016/j.rser.2007.01.023.
[6] M. Thackeray M, Wolverton C, D. Isaacs E. Electrical energy storage for transportation—approaching the limits of, and going beyond, lithium-ion batteries. Energy & Environmental Science 2012;5:7854–63. 10.1039/C2EE21892E.
[7] Byrne RH, Nguyen TA, Copp DA, Chalamala BR, Gyuk I. Energy management and optimization methods for grid energy storage systems. IEEE Access 2018;6:13231–60. https://doi.org/10.1109/ACCESS.2017.2741578.
[8] Peters IM, Breyer C, Jaffer SA, Kurtz S, Reindl T, Sinton R, et al. The role of batteries in meeting the PV terawatt challenge. Joule 2021;5:1353–70. https://doi.org/10.1016/j.joule.2021.03.023.
[9] Yang T, Liu W, Kramer GJ, Sun Q. Seasonal thermal energy storage: a techno-economic literature review. Renew Sustain Energy Rev 2021;139:110732. https://doi.org/10.1016/j.rser.2021.110732.
[10] Lai CS, Locatelli G, Pimm A, Wu X, Lai LL. A review on long-term electrical power system modeling with energy storage. J Clean Prod 2021;280:124298. https://doi.org/10.1016/j.jclepro.2020.124298.
[11] Heidari M, Parra D, Patel MK. Physical design, techno-economic analysis and optimization of distributed compressed air energy storage for renewable energy integration. J Storage Mater 2021;35:102268. https://doi.org/10.1016/j.est.2021.102268.
[12] Gaudard L. Pumped-storage project: a short to long term investment analysis including climate change. Renew Sustain Energy Rev 2015;49:91–9. https://doi.org/10.1016/j.rser.2015.04.052.
[13] Blanco H, Faaij A. A review at the role of storage in energy systems with a focus on Power to Gas and long-term storage. Renew Sustain Energy Rev 2018;81:1049–86. https://doi.org/10.1016/j.rser.2017.07.062.
[14] Gao D, Kwan TH, Dabwan YN, Hu M, Hao Y, Zhang T, et al. Seasonal-regulatable energy systems design and optimization for solar energy year-round utilization☆. Appl Energy 2022;322:119500. https://doi.org/10.1016/j.apenergy.2022.119500.
[15] Yuan X, Heikari L, Hirvonen J, Liang Y, Virtanen M, Kosonen R, et al. System modelling and optimization of a low temperature local hybrid energy system based on solar energy for a residential district. Energ Conver Manage 2022;267:115918. https://doi.org/10.1016/j.enconman.2022.115918.
[16] Zeyen E, Hagenmeyer V, Brown T. Mitigating heat demand peaks in buildings in a highly renewable European energy system. Energy 2021;231:120784. https://doi.org/10.1016/j.energy.2021.120784.
[17] van der Heijde B, Vandermeulen A, Salenbien R, Helsen L. Representative days selection for district energy system optimisation: a solar district heating system with seasonal storage. Appl Energy 2019;248:79–94. https://doi.org/10.1016/j.apenergy.2019.04.030.
[18] Gabrielli P, Gazzani M, Martelli E, Mazzotti M. Optimal design of multi-energy systems with seasonal storage. Appl Energy 2018;219:408–24. https://doi.org/10.1016/j.apenergy.2017.07.142.
[19] Petkov I, Gabrielli P, Spokaite M. The impact of urban district composition on storage technology reliance: trade-offs between thermal storage, batteries, and power-to-hydrogen. Energy 2021;224:120102. https://doi.org/10.1016/j.energy.2021.120102.
[20] Li Z, Xu Y, Feng X, Wu Q. Optimal stochastic deployment of heterogeneous energy storage in a residential multienergy microgrid with demand-side management.

IEEE Trans Ind Inf 2021;17:991–1004. https://doi.org/10.1109/TII.2020.2971227.

[21] Flores-Quiroz A, Strunz K. A distributed computing framework for multi-stage stochastic planning of renewable power systems with energy storage as flexibility option. Appl Energy 2021;291:116736. https://doi.org/10.1016/j.apenergy.2021.116736.

[22] Dantzig GB, Wolfe P. Decomposition principle for linear programs. Oper Res 1960;8:101–11. https://doi.org/10.1287/opre.8.1.101.

[23] Perera ATD, Nik VM, Chen D, Scartezzini J-L, Hong T. Quantifying the impacts of climate change and extreme climate events on energy systems. Nat Energy 2020;5:150–9. https://doi.org/10.1038/s41560-020-0558-0.

[24] Nik VM, Perera ATD, Chen D. Towards climate resilient urban energy systems: a review. Natl Sci Rev 2020. https://doi.org/10.1093/nsr/nwaa134.

[25] Gao L, Zhao J, An Q, Wang J, Liu X. A review on system performance studies of aquifer thermal energy storage. Energy Procedia 2017;142:3537–45. https://doi.org/10.1016/j.egypro.2017.12.242.

[26] Lee KS. A review on concepts, applications, and models of aquifer thermal energy storage systems. Energies 2010;3:1320–34. https://doi.org/10.3390/en3061320.

[27] Fleuchaus P, Schüppler S, Godschalk B, Bakema G, Blum P. Performance analysis of Aquifer Thermal Energy Storage (ATES). Renew Energy 2020;146:1536–48. https://doi.org/10.1016/j.renene.2019.07.030.

[28] Wesselink M, Liu W, Koornneef J, van den Broek M. Conceptual market potential framework of high temperature aquifer thermal energy storage – a case study in the Netherlands. Energy 2018;147:477–89. https://doi.org/10.1016/j.energy.2018.01.072.

[29] Rostampour V, Jaxa-Rozen M, Bloemendal M, Kwakkel J, Keviczky T. Aquifer Thermal Energy Storage (ATES) smart grids: Large-scale seasonal energy storage as a distributed energy management solution. Appl Energy 2019;242:624–39. https://doi.org/10.1016/j.apenergy.2019.03.110.

[30] van der Roest E, Snip L, Fens T, van Wijk A. Introducing Power-to-H3: Combining renewable electricity with heat, water and hydrogen production and storage in a neighbourhood. Appl Energy 2020;257:114024. https://doi.org/10.1016/j.apenergy.2019.114024.

[31] Kubiński K, Szabłowski Ł. Dynamic model of solar heating plant with seasonal thermal energy storage. Renew Energy 2020;145:2025–33. https://doi.org/10.1016/j.renene.2019.07.120.

[32] Mauree D, Naboni E, Coccolo S, Perera ATD, Nik VM, Scartezzini J-L. A review of assessment methods for the urban environment and its energy sustainability to guarantee climate adaptation of future cities. Renew Sustain Energy Rev 2019;112:733–46. https://doi.org/10.1016/j.rser.2019.06.005.

[33] Perera ATD, Wickremasinghe DMIJ, Mahindarathna DVS, Attalage RA, Perera KKCK, Bartholameuz EM. Sensitivity of internal combustion generator capacity in standalone hybrid energy systems. Energy 2012;39:403–11. https://doi.org/10.1016/j.energy.2011.12.039.

[34] Durisch W, Bitnar B, Mayor J-C, Kiess H, Lam K, Close J. Efficiency model for photovoltaic modules and demonstration of its application to energy yield estimation. Sol Energy Mater Sol Cells 2007;91:79–84. https://doi.org/10.1016/j.solmat.2006.05.011.

[35] Downing SD, Socie DF. Simple rainflow counting algorithms. Int J Fatigue 1982;4:31–40. https://doi.org/10.1016/0142-1123(82)90018-4.

[36] Bloemendal M, Hartog N. Analysis of the impact of storage conditions on the thermal recovery efficiency of low-temperature ATES systems. Geothermics 2018;71:306–19. https://doi.org/10.1016/j.geothermics.2017.10.009.

[37] Rezvani A, Khalili A, Mazareie A, Gandomkar M. Modeling, control, and simulation of grid connected intelligent hybrid battery/photovoltaic system using new hybrid fuzzy-neural method. ISA Transactions n.d. 10.1016/j.isatra.2016.02.013.

[38] Safari S, Ardehali MM, Sirizi MJ. Particle swarm optimization based fuzzy logic controller for autonomous green power energy system with hydrogen storage. Energ Conver Manage 2013;65:41–9. https://doi.org/10.1016/j.enconman.2012.08.012.

[39] Berrazouane S, Mohammedi K. Parameter optimization via cuckoo optimization algorithm of fuzzy controller for energy management of a hybrid power system. Energ Conver Manage 2014;78:652–60. https://doi.org/10.1016/j.enconman.2013.11.018.

[40] Athari MH, Ardehali MM. Operational performance of energy storage as function of electricity prices for on-grid hybrid renewable energy system by optimized fuzzy logic controller. Renew Energy 2016;85:890–902. https://doi.org/10.1016/j.renene.2015.07.055.

[41] Olatomiwa L, Mekhilef S, Ismail MS, Moghavvemi M. Energy management strategies in hybrid renewable energy systems: a review. Renew Sustain Energy Rev 2016;62:821–35. https://doi.org/10.1016/j.rser.2016.05.040.

[42] Perera ATD, Nik VM, Mauree D, Scartezzini J-L. Electrical hubs: An effective way to integrate non-dispatchable renewable energy sources with minimum impact to the grid. Appl Energy 2017;190:232–48. https://doi.org/10.1016/j.apenergy.2016.12.127.

[43] Perera ATD, Nik VM, Mauree D, Scartezzini J-L. An integrated approach to design site specific distributed electrical hubs combining optimization, multi-criterion assessment and decision making. Energy 2017;134:103–20. https://doi.org/10.1016/j.energy.2017.06.002.

[44] Narayan A, Ponnambalam K. Risk-averse stochastic programming approach for microgrid planning under uncertainty. Renew Energy 2017;101:399–408. https://doi.org/10.1016/j.renene.2016.08.064.

[45] Rezvan AT, Gharneh NS, Gharehpetian GB. Optimization of distributed generation capacities in buildings under uncertainty in load demand. Energ Build 2013;57:58–64. https://doi.org/10.1016/j.enbuild.2012.10.031.

[46] Sharafi M, ElMekkawy TY. Stochastic optimization of hybrid renewable energy systems using sampling average method. Renew Sustain Energy Rev 2015;52:1668–79. https://doi.org/10.1016/j.rser.2015.08.010.

[47] Urbanucci L, Testi D. Optimal integrated sizing and operation of a CHP system with Monte Carlo risk analysis for long-term uncertainty in energy demands. Energ Conver Manage 2018;157:307–16. https://doi.org/10.1016/j.enconman.2017.12.008.

[48] Gu W, Tang Y, Peng S, Wang D, Sheng W, Liu K. Optimal configuration and analysis of combined cooling, heating, and power microgrid with thermal storage tank under uncertainty. J Renew Sustain Energy 2015;7:013104. https://doi.org/10.1063/1.4904434.

[49] Lund PD, Lindgren J, Mikkola J, Salpakari J. Review of energy system flexibility measures to enable high levels of variable renewable electricity. Renew Sustain Energy Rev 2015;45:785–807. https://doi.org/10.1016/j.rser.2015.01.057.

[50] Kondziella H, Bruckner T. Flexibility requirements of renewable energy based electricity systems – a review of research results and methodologies. Renew Sustain Energy Rev 2016;53:10–22. https://doi.org/10.1016/j.rser.2015.07.199.

[51] Perera ATD, Nik VM, Wickramasinghe PU, Scartezzini J-L. Redefining energy system flexibility for distributed energy system design. Appl Energy 2019;253:113572. https://doi.org/10.1016/j.apenergy.2019.113572.

[52] Mimw. Measuring machine and product mix flexibilities of a manufacturing system. Int J Prod Res 2005;43:3773–86. https://doi.org/10.1080/00207540500147091.

[53] Das SK. The measurement of flexibility in manufacturing systems. Int J Flex Manuf Syst n.d.;8:67–93. 10.1007/BF00167801.

[54] Bajpai P, Dash V. Hybrid renewable energy systems for power generation in stand-alone applications: a review. Renew Sustain Energy Rev 2012;16:2926–39. https://doi.org/10.1016/j.rser.2012.02.009.

[55] Erdinc O, Uzunoglu M. Optimum design of hybrid renewable energy systems: overview of different approaches. Renew Sustain Energy Rev 2012;16:1412–25. https://doi.org/10.1016/j.rser.2011.11.011.

[56] Bernal-Agustín JL, Dufo-López R. Efficient design of hybrid renewable energy systems using evolutionary algorithms. Energ Conver Manage 2009;50:479–89. https://doi.org/10.1016/j.enconman.2008.11.007.

[57] Alba E, Tomassini M. Parallelism and evolutionary algorithms. IEEE Trans Evol Comput 2002;6:443–62. https://doi.org/10.1109/TEVC.2002.800880.

[58] Zhang Y, Wang S, Ji G. A Comprehensive survey on particle swarm optimization algorithm and its applications. Math Probl Eng 2015. https://doi.org/10.1155/2015/931256.

[59] Laumanns M, Thiele L, Deb K, Zitzler E. Combining convergence and diversity in evolutionary multiobjective optimization. Evol Comput 2002;10:263–82. https://doi.org/10.1162/106365602760234108.

[60] Ballarini I. Splitting global solar radiation into diffuse & direct using Excel 2020.

[61] hobob0t, cwmande. psychropy. UC Davis; 2022.